Journal of Petroleum Science and Engineering 179 (2019) 378–393

Contents lists available at ScienceDirect

Journal of Petroleum Science and Engineering

journal homepage: www.elsevier.com/locate/petrol

Analysis of stress interference among multiple hydraulic fractures using a fully three-dimensional displacement discontinuity method

Huiying Tang[a,*], Shihao Wang[b], Ruihan Zhang[a], Sanbai Li[c], Liehui Zhang[a], Yu-Shu Wu[b]

[a] State Key Laboratory of Oil and Gas Reservoir Geology and Exploitation, Southwest Petroleum University, Chengdu, 610500, PR China
[b] Department of Petroleum Engineering, Colorado School of Mines, Golden, CO, 80401, USA
[c] Key Laboratory of Ministry of Education on Safe Mining of Deep Metal Mines, Northeastern University, Shenyang, 110819, PR China

ARTICLE INFO

Keywords:
Hydraulic fracturing
Multiple fracture propagation
Stress interference
Three-dimensional displacement discontinuity method

ABSTRACT

Due to the extremely low permeability of shale matrix, a great number of hydraulic fractures are required to enhance the flow capacity of shale reservoirs to obtain economic productivity. The mechanical interactions among closely spaced hydraulic fractures could result in fracture curving, intersection and unbalanced growth. Current hydraulic fracturing models are mainly based on the assumption of 2D or Pseudo-3D, in which the fractures are vertical with constant or equilibrium height. To better analyze and understand the stress interference among multiple hydraulic fractures, a fully three-dimensional (3D) model based on the displacement discontinuity method (DDM) is developed in this paper. The challenges (eq. grid twisting, hyper-singular integrals) in implementing 3D DDM for fracture growth problems are systematically discussed and solved from different aspects. Optimization strategies for the 3D model, including adaptive mesh growth, non-crowding Gaussian points and distance-dependent integrals, are proposed. Using this model, we first compare the strength of stress interactions with different fracture geometries. The simulation results show that the length of the shorter edge of the hydraulic fracture dominates the strength of stress shadowing effect. The stress redistribution due to fracture interference in 3D space is also calculated which delivers a much more complex shape of potentially stress re-orientation region than the 2D results. Then, the simultaneous propagation of multiple hydraulic fractures in different *in-situ* stress fields is analyzed, highlighting the importance of *in-situ* stress distribution on fracture geometries and interactions. The limitation on fracture height growth can reduce the mechanical interactions under the constant net pressure assumption. Besides, the detailed introduction of the present stable and efficient 3D DDM-based fracture propagation model can be used as a basis for other investigation purposes.

1. Introduction

The investigations of stress interactions among multiple propagating fractures started from the 1990s when the geologists observed special patterns of closely spaced joints (echelons, wing-cracks, etc.) in out-crops (Olson, 1993; Pollard and Aydin, 1988). The importance of fracture interference grew in early 2000s when multi-stage hydraulic fracturing technology showed its significant role in enhancing shale gas production (Miller et al., 2011). The continuous development of fracking technologies allows smaller cluster spacing (usually taken as fracture spacing) to extend the fracture surface area, thus higher production rate can be achieved. Currently, the cluster spacing can be as close as 15 ft in Eagle Ford and DJ basins, and even closer spacing is under test (Xiong, 2017). With the decrease of fracture distance, the interactions among hydraulic fractures can no longer be ignored (Geyer and Nemat-Nasser, 1982; Abass et al., 1996; Miller et al., 2011; Dohmen et al., 2014). The fracture interactions in hydraulic fracturing process have been extensively studied with emerging methods in the past decade (Peirce and Bunger, 2013; Wu and Olson, 2016; Li et al., 2016).

Currently, theoretical and numerical studies on multiple fracture propagation problems are mainly based on the assumptions of 2D, Pesudo-3D or Planar-3D. Two dimensional analysis of the unbalanced growth of middle and side fractures due to stress shadowing effect have been conducted by Cheng (2012) and Liu et al. (2016) with displacement discontinuity method (DDM) and extended finite element method (XFEM), respectively. The displacement discontinuity method (DDM) is an indirect boundary element method which solves the displacement discontinuities on domain boundaries to get the rest of the variables. Wu and Olson (2016) investigated the fracture deflection and uneven

* Corresponding author. author.
E-mail address: tanghuiying@swpu.edu.cn (H. Tang).

https://doi.org/10.1016/j.petrol.2019.04.050
Received 27 November 2018; Received in revised form 1 March 2019; Accepted 14 April 2019
Available online 25 April 2019

growth due to the combined effect of wellbore flow partitioning and mechanical interference with a constant height 2D DDM model. A series of Pseudo-3D models, capable of describing the fracture height growth without increasing unknowns in the vertical direction, have been developed recently (Weng et al., 2011; Dontsov and Peirce, 2015; Liu and Valkó, 2018). A stacked height model proposed by Cohen et al. (2017) could partially solve the limitations of the previous Pseudo-3D models in handling complex heterogeneity of *in-situ* stresses, but extra elements should be placed in locally minimum stress layers. The Planar-3D models, which constrain the deflection of fracture plane while allowing two-dimensional flows, provide better description of fluid and proppant behaviors inside the fractures. The Planar-3D simulation of multiple fracture propagation with finite element method (FEM) conducted by Peirce and Bunger (2013) highlights the effectiveness of non-uniform placement of perforation clusters on increasing fracture surface area. Bunger (2013) proposed a semi-analytical method based on the energy equilibrium for describing the propagation of multiple planar fractures. With this method, they found that the dimensionless cluster space 1.5H (fracture height) and 2.5H are the optimal spacing for the strong perforation losses and zero perforation losses (Bunger et al., 2014). Tang et al. (2016) investigated the impact of stress interference on proppant partitioning among multiple fractures with Planar-3D DDM and severe unbalanced distribution of proppant was observed. One major limitation of the Planar-3D models is that they cannot consider the fracture curving caused by stress interactions or *in-situ* stress heterogeneity. Therefore, to achieve more realistic description of the fracture propagation process, several recent efforts have been made for modeling multiple fracture propagation in three-dimension (Li et al. 2012, 2016; Wick et al., 2015; Kumar and Ghassemi, 2015; Haddad and Sepehrnoori, 2016; Dehghan et al., 2017).

The combination of Extended Finite Element Method (XFEM) and Cohesive Zone Method (CZM) had been adopted to investigate the 3D hydraulic fracturing problems (Haddad and Sepehrnoori, 2016; Dehghan et al., 2017), as well as the 3D damage based model (Li et al., 2012), phase field model (Wick et al., 2015) and pseudo-continua model (Li et al., 2016). Due to the capability in treating arbitrary fracture shapes with high efficiency by reducing model dimension, the boundary element method (BEM) became an attractive tool for fracture problems. Castonguay et al. (2013) investigated the geometric evolution of simultaneously propagating fractures in anisotropic stresses using symmetric Galerkin BEM. Kumar and Ghassemi (2015) proposed a 3D poroelastic DDM with utilization of quadrilateral elements to study the impact of stress shadowing effect on simultaneously and sequential propagating fractures. The triangular grid based BEM developed by Maerten et al. (2014) was used to investigate the mixed-mode fracture propagation, including the mode III fractures, under tensile and shearing stresses.

Though the advantages of boundary element method in 3D simulation are widely recognized, the difficulties in its implementation have not been fully resolved. Taken DDM as an example, several challenges are frequently encountered when conducting 3D simulations, especially on triangular elements. The first challenge is the calculation of influence coefficients in mechanical equations. The calculation of the influence coefficients with hyper, strong and weak-singular integrals on arbitrarily shaped triangular elements is much more challenging than 2D line segments (Crouch et al., 1983; Shou and Crouch, 1995) or 3D rectangular elements (Shou et al., 1998). The use of analytical expressions of influence coefficients can effectively accelerate the calculation (Kuriyama and Mizuta, 1993; Nikolskiy et al., 2013; Cheng et al., 2015), but their extensions to more complex formulations (e.g. tip elements (Li et al., 2001)) is quite difficult. Besides, the derived expressions are often too complex to be used by other researchers and the analytical solutions could be invalid at certain locations (Shi et al., 2014). Thus, an effective numerical solution is desired. Various methods have been developed to evaluate the singular integrals numerically. For example, the singularity-reduced method developed by Li and Mear (1998), which turns the hyper or strongly singular kernel functions into weakly-singular integrals, has been applied in a three dimensional finite element model to solve fracture propagation problems (Rungamornrat et al., 2005). A method capable of formulating the boundary integral equations with kernels of any order of singularity is proposed by Guiggiani et al. (1992), which calculates the singular integrals directly without solving in the Cauchy principal value or finite part sense. Zozulya (2007) transformed the singular integrals into the easily calculated regular contour integrals based on the theory of distribution and application of the Green theorem. A triangle subdividing technique, developed from Guiggiani's method, is applied in this work. For the non-singular integrals, the non-crowding Gaussian integration points (Hussain et al., 2012) and adaptive adjustment of integral point number are adopted in this paper to improve model accuracy and efficiency.

On the other side, when the element-wise propagation strategy is used, the severe skewness of fracture front may occur (Shi et al., 2014). To the authors’ knowledge, few research on 3D DDM has dealt with the grid twisting issues generated from the growing cracks surface after a few steps of propagation, especially for the case of strong *in-situ* stress heterogeneity. The adaptive adjustment of grid geometry has been applied in several 3D FEM models (Yew and Weng, 2015; Gupta and Duarte, 2018), in which the re-meshing should be conducted after each propagating step with grid refined around the fracture tips. However, due to the cost of influence coefficients computation, globally re-meshing is not expected in DDM. For this reason, a partial re-meshing strategy which regenerates grids within a zone surrounding fracture tips was proposed by Rungamornrat et al. (2005). In this paper, an adaptive mesh adjustment method with few re-meshing is proposed which effectively avoid bad-quality grids by conducting a series of operations.

To solve the above issues, we first derive the formulations of three dimensional DDM for triangular elements. The calculations of singular and non-singular integrals in influence coefficients are introduced. Numerical methods including coordinates transformation, non-crowding Gaussian integration points and distance dependent integrals are integrated in our model to ensure the accuracy of the integral calculation. Several grid adjustment operations to avoid skewed fracture front elements are proposed and tested. Using the developed 3D model, we compare the strength of stress interactions among multiple hydraulic fractures with different geometries. Finally, the impact of the heterogeneity of three dimensional *in-situ* stresses on multiple fracture propagation is investigated.

2. Methods

In this work, we seek the solution of the 3D elasticity equations for propagating hydraulic fractures in a reservoir assumed to be linear elastic. The coupling between the elasticity and flow equations in the reservoir or in the fracture is not considered. The fluid pressure applied on the fracture surfaces is assumed to be constant in each time step. Under these assumptions, we first derive the integral forms of the influence coefficients. Then, the methods for the singular and non-singular integral calculations are provided. Last, the grid quality control strategies used during fracture propagation process are introduced and tested.

2.1. 3D DDM formulations

The displacement discontinuity method (DDM) is an indirect boundary element method, which calculates the displacement discontinuities on domain boundaries as indirect variables to derive the stresses, strains and displacements at any given locations. In our model, the fracture surface is first divided into a bunch of planar triangles as shown in Fig. 1. The local coordinate system is defined that the x axis is parallel to the longest edge and the axis z is normal to the element plane. Constant element is used in this paper which assumes the

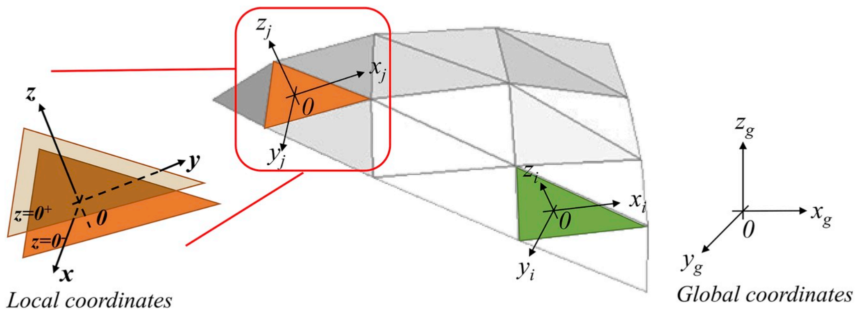

Fig. 1. Schematics of the local (x_i-y_i-z_i) and global (x_g-y_g-z_g) coordinates of 3D fracture elements.

displacement discontinuities to be invariable across each element, and the unknowns are located in the element center of gravity. Based on these assumptions, each element has three displacement discontinuities to be solved in the local coordinate system (x-y-z), which are defines as:

$$\begin{aligned} D_x &= u_x(x, y, 0^-) - u_x(x, y, 0^+) \\ D_y &= u_y(x, y, 0^-) - u_y(x, y, 0^+) \\ D_z &= u_z(x, y, 0^-) - u_z(x, y, 0^+) \end{aligned} \tag{1}$$

where u is the displacement, superscripts + and - indicate values on the positive and negative side of the fracture, D_x and D_y are shearing displacement discontinuities along x and y directions respectively, and D_z is the normal displacement between lower and upper surfaces, which is negative when fracture opens.

The stresses induced by each element at source point (x,y,z) can be calculated with the following expressions (Okada, 1985),

$$\begin{aligned} u_x &= C\{[2(1-\nu)I_{,z} - zI_{,xx}]D_x - zI_{,xy}D_y - [(1-2\nu)I_{,x} + zI_{,xz}]D_z\} \\ u_y &= C\{-zI_{,xy}D_x + [2(1-\nu)I_{,z} - zI_{,yy}]D_y - [(1-2\nu)I_{,y} + zI_{,yz}]D_z\} \\ u_x &= C\{[(1-2\nu)I_{,x} - zI_{,xz}]D_x + [(1-2\nu)I_{,y} - zI_{,yz}]D_y \\ &\quad + [2(1-\nu)I_{,z} - zI_{,zz}]D_z\} \\ \sigma_{xx} &= 2C\{[2I_{,xz} - zI_{,xxx}]D_x + [2\nu I_{,yz} - zI_{,xxy}]D_y \\ &\quad + [I_{,zz} + (1-2\nu)I_{,yy} - zI_{,xxz}]D_z\} \\ \sigma_{yy} &= 2C\{[2\nu I_{,xz} - zI_{,xyy}]D_x + [2I_{,yz} - zI_{,yyy}]D_y \\ &\quad + [I_{,zz} + (1-2\nu)I_{,xx} - zI_{,yyz}]D_z\} \\ \sigma_{zz} &= 2C\{-zI_{,xzz}D_x - zI_{,yzz}D_y + [I_{,zz} - zI_{,zzz}]D_z\} \\ \tau_{xy} &= 2C\{[(1-\nu)I_{,yz} - zI_{,xxy}]D_x + [(1-\nu)I_{,xz} - zI_{,xyy}]D_y \\ &\quad - [(1-2\nu)I_{,xy} + zI_{,xyz}]D_z\} \\ \tau_{yz} &= 2C\{-[\nu I_{,xy} + zI_{,xyz}]D_x + [I_{,zz} + \nu I_{,xx} - zI_{,yyz}]D_y - zI_{,yzz}D_z\} \\ \tau_{zx} &= 2C\{[I_{,zz} + \nu I_{,yy} - zI_{,xxz}]D_x - [\nu I_{,xy} + zI_{,xyz}]D_y - zI_{,xzz}D_z\} \end{aligned} \tag{2}$$

in which C is a constant calculated from Poisson's ratio ν:

$$C = \frac{1}{8\pi(1-\nu)} \tag{3}$$

Kernel function I in Eq. (2) is a surface integral over each element's local coordinates,

$$I(x, y, z) = \iint_{\Delta} [(x-\xi)^2 + (y-\eta)^2 + z^2]^{-1/2} d\xi d\eta \tag{4}$$

and I_k, I_{kl} and I_{klm} are first, second and third order derivatives of coordinate k, l and m. For hydraulic fractures, the force equilibrium for element i can be written as,

$$\sigma_{in}^i = \sigma_{induce}^i + \sigma_0^i \tag{5}$$

where the subscript *in* means the internal boundary stress (i.e. fluid pressure) calculated from flow equations, *induce* denotes the stresses induced by the deformations of all fracture elements and 0 means the *in-situ* stresses. The induced shear and normal stresses at the midpoint of the ith element can be obtained by summing up the contribution of each set of discontinuity over N elements as:

$$\begin{aligned} \tau_{induce,x}^i &= \textstyle\sum_j^N A_{xx}^{ij} D_x^j + \sum_j^N A_{xy}^{ij} D_y^j + \sum_j^N A_{xz}^{ij} D_z^j \\ \tau_{induce,y}^i &= \textstyle\sum_j^N A_{yx}^{ij} D_x^j + \sum_j^N A_{yy}^{ij} D_y^j + \sum_j^N A_{yz}^{ij} D_z^j \\ \sigma_{induce,z}^i &= \textstyle\sum_j^N A_{zx}^{ij} D_x^j + \sum_j^N A_{zy}^{ij} D_y^j + \sum_j^N A_{zz}^{ij} D_z^j \end{aligned} \tag{6}$$

The coefficients A^{ij}, usually called the influence coefficients, can be derived from Eq. (2) with coordinate transformations. The analytical expressions of A^{ij} of rectangular element have been provided by Shou et al. (1998) and revisited by Wu (2014). Analytical solutions of triangles can be found in Kuriyama and Mizuta (1993) for constant element and Cheng et al. (2015) for linear element. As discussed before, the focus of this paper is to use numerical ways to solve A^{ij} for its simplicity and versatility. In the following sections, we'll introduce how the singular and non-singular integrals can be calculated numerically.

2.2. Numerical calculation of influence coefficients

The numerical evaluation of singular integrals on triangular boundary elements that arises in the 3D boundary element method when the source point is on or very close to the element of integration is always a challenge in simulations. In this section, the methods for singular and non-singular integral calculations will be introduced separately. The issues related to the choice of the location and the number of integration points will also be discussed.

2.2.1. Singular-integral calculation

In DDM, if the source point is located on the element's gravity center, such as the calculation of self-influence coefficient (A^{ii}), different orders of singularities (weakly singular ($1/|r|$), strongly singular ($1/|r^2|$) and hypersingular($1/|r^3|$)) could occur in the derivatives of kernel function I. Various methods have been developed to deal with these singular integrals, such as polar coordinate transformation (Rizzo and Shippy, 1977), non-linear transformation techniques (Lachat and Watson, 1976), and regularization of boundary integral equation (Li and Huang, 2010). The above methods require an integration over the complete surface, resulting in high numerical complexity and time cost. The integration scheme presented by Guiggiani et al. (1992) can be used for any order of singularity which transfers the singular surface integral into a regular line integral, avoiding the use of a large number of integral points. In this paper, an integration procedure with a two-step coordinate transformation and integration by parts are adopted, which could conveniently simplify the singular integrals into regular line integrals. The calculation of a third order singular integral is taken as an example and shown in Appendix A. After a series of transformations, the singular integrals can be written as the summation of line integrals over each sub-triangle shown in Fig. 21,

$$\sum_i^3 2A_i \int_0^1 g(\varepsilon_i) d\varepsilon_i \tag{7}$$

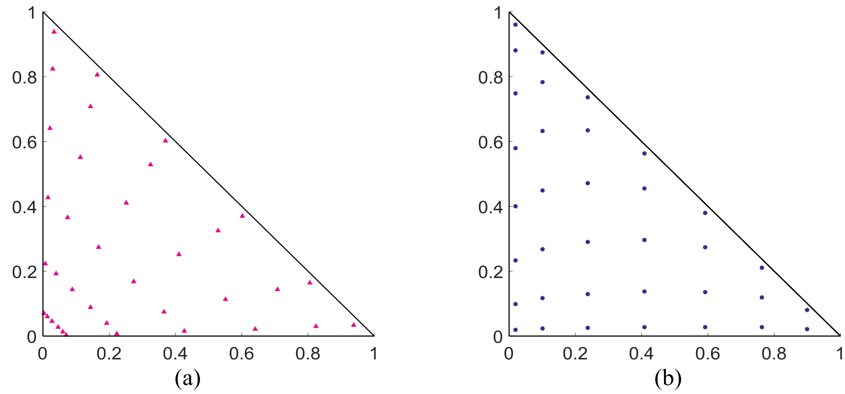

Fig. 2. (a) Example of n × n Gaussian points; and (b) Example of non-crowding n(n + 1)/2 Gaussian points (n = 6 in the above example).

where A_i is the area of the sub-triangleΔ_i, the expression of $g(\varepsilon_i)$ can be found in Eq. (A.10) in Appendix A.

2.2.2. Non-singular integrals

When the source point moves way from the cell centers, the integrals become regular and can be directly evaluated with Gaussian integration algorithms. However, the choice of location and number of integral points is critical for the model accuracy and efficiency. In this paper, a new quadrature formula technique proposed by Hussain et al. (2012) is applied which avoids the crowding of Gaussian points by using of simple algorithms. The traditional one dimensional n-point Gaussian quadrature requires n × n integration points and often clustered around the triangle vertex (Fig. 2(a)), while this new technique generates only n(n + 1)/2 points with Gaussian points evenly distributed in the integral area (Fig. 2(b)).

To verify the effectiveness of this method in our problem, we compare the numerical evaluations of the integrals in Eq. (2) with the analytical solutions for rectangular boundary element (Wu, 2014), where the rectangle is divided into four triangles as shown in Fig. 3. The source points are perpendicular to or in-plane with the rectangular surface. The red dots in Fig. 3 denote the source points and the relative error of numerical integration is defined as:

$$error = \max\left(\frac{|I_{num,i} - I_{ana,i}|}{|I_{ana,i}|}\right),\ i = 1,2....16 \tag{8}$$

The subscript *ana* represents the analytical solutions and *num* denotes numerical results. *i* ranges from 1 to 16 denoting the 16 derivatives of kernal function *I* in Eq. (2). The number of integral points required to achieve tolerance 10^{-3} is calculated and compared.

For a square unit, 9 source points (Fig. 3) are calculated using one dimensional n-point Gaussian quadrature (resulting in n × n Gaussian points) and non-crowding formulas (n(n + 1)/2 points). The number of integral points required to get the same accuracy is listed Table 1. As shown in Table 1, the closer the points are to the element, the more integral points are needed. For the closer source points, non-crowding method performs better, while the crowding method performs slightly better for points that are farther away. When skewing the geometry of integral domain by doubling the height (b = 2a), the non-crowding method always requires less integrations. Since the shape of fracture element varies during propagation, this non-crowding method could provide more stable results compared to the traditional quadrature formulas.

As shown in Table 1, more points are required when the shape of element diverts from equilateral triangle, which is also true for the singular integral calculations. The change of integral points number with increasing ratio of a/b is displayed in Table 2. With good control of grid quality, the ratio can be expected to below 3. Thus, the point number for 1D singular integrals is chosen to be 17 × 3 in this work.

The effectiveness of non-crowding Gaussian points is further tested with fracture opening calculation. The analytical solution of the width of a pressurized radial fracture is (Sneddon 1946),

$$w = \frac{8p_0(1-\nu^2)}{\pi E}(c^2 - r^2)^{1/2} \tag{9}$$

where E is the Young's modulus, ν is the Poisson's ratio, c is the radius of fracture, p_0 is the net pressure and r is the radial distance from fracture center. In this case, E = 20 GPa, ν = 0.25, c = 1m and p_0 = 2 MPa.

As demonstrated in Fig. 4, with the same number of integral points, the non-crowding algorithm can match the analytical solution better,

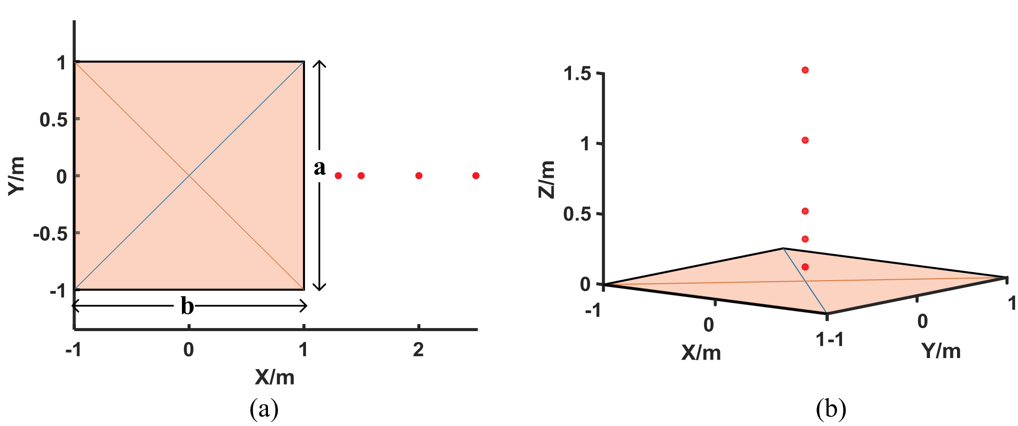

Fig. 3. (a) Source points (red dot) in *x-y* planes with *x* varies from 1.3 to 2.5 and *y* = 0; and (b) Out of plane integration points with *x* = 0, *y* = 0, *z* = 0.1, 0.3, 0.5, 1.0, 1.5. (For interpretation of the references to color in this figure legend, the reader is referred to the Web version of this article.)

Table 1
Number of integration points required to satisfy the error tolerance.

Algorithm	Number of integral points required at location (x,y,z)								
	$x = 1.3$ $y = 0$ $z = 0$	$x = 1.5$ $y = 0$ $z = 0$	$x = 2$ $y = 0$ $z = 0$	$x = 2.5$ $y = 0$ $z = 0$	$x = 0$ $y = 0$ $z = 0.1$	$x = 0$ $y = 0$ $z = 0.3$	$x = 0$ $y = 0$ $z = 0.5$	$x = 0$ $y = 0$ $z = 1.0$	$x = 0$ $y = 0$ $z = 1.5$
Geometry: a = b									
n × n points	324	121	25	16	529	144	36	25	16
n(n+1)/2 points	170	77	54	54	324	65	44	35	27
Geometry: b = 2a									
n × n points	841	196	100	49	36	1225	441	100	49
n(n+1)/2 points	464	119	65	35	35	629	230	65	54

especially in the central parts where the length of the element edges differs the most (Fig. 4(b)), which is consistent with the conclusion we have drawn from Table 1. To further increase the computing efficiency, a distance-based adjustment of the number of integration points is adopted with the following equations:

$$\begin{cases} n = 21, & , \quad e \le 0.5 \\ n = 8 + \frac{2.5}{21-8}e, & 0.5 < e < 3\,, \quad e = \dfrac{D}{L_{\max}} \\ n = 8 & , \quad e \ge 3 \end{cases} \tag{10}$$

In which, D is the distance between source points and element center, L_{max} is the longest edge of current element and the actual number of integration points is n(n+1)/2 when using the non-crowding algorithm. The variable e represents how close the source point and element are and the smaller e is, more integration points are needed.

2.3. Fracture propagation modeling

In our model, the maximum principal stress criterion proposed by Schöllmann et al. (2002) is adopted to determine the fracture propagation directions, which is able to predict both kink and twisted angles so that the mixed mode I/II/III fractures can be modelled. The maximum principal stress ahead of the fracture tip can be calculated in the local polar coordinates (Fig. 5) with the equation below,

$$\sigma_1 = \frac{\sigma_\theta + \sigma_z}{2} + \frac{1}{2}\sqrt{(\sigma_\theta - \sigma_z)^2 + 4\tau_{\theta z}^2} \tag{11}$$

where the tangential stressσ_θ, vertical stress$\sigma_z$and shear stress $\tau_{\theta z}$can be evaluated with stress intensity factors K_I, K_{II} and K_{III} (Safari and Ghassemi 2016) as,

$$\begin{aligned} \sigma_\theta &= \frac{K_I}{\sqrt{2\pi r}}\left[3\cos\left(\frac{\theta}{2}\right) + \cos\left(\frac{3\theta}{2}\right)\right] - \frac{K_{II}}{\sqrt{2\pi r}}\left[3\sin\left(\frac{\theta}{2}\right) + \sin\left(\frac{3\theta}{2}\right)\right] \\ \tau_{\theta z} &= \frac{K_{III}}{\sqrt{2\pi r}}\cos\left(\frac{\theta}{2}\right) \\ \sigma_z &= \frac{\sigma_\theta}{2} + \frac{1}{2}\sqrt{(\sigma_\theta{}^2 + 4\tau_{\theta z}{}^2)} \end{aligned} \tag{12}$$

in which r is the distance from source point to fracture front, θ is the kink angle as defined in Fig. 5, and the stress intensity factors can be calculated with the displacement discontinuities D_i of the tip elements as follows:

$$K_i = \frac{0.806E\sqrt{\pi}}{4(1-\nu^2)\sqrt{2r}}D_i,\ i = x, y, z \tag{13}$$

The constant 0.806 was originally determined empirically by Olson (1991) in 2D problems who found the stress intensity factors calculated using DDM is generally larger than analytical solutions. The value of 0.806 was then used by McClure et al. (2016) for rectangular elements which matches well with the PKN and KGD fracture analytical solutions. Kumar and Ghassemi (2015) takes $r = 0.87L$ for rectangular element where L is the full length of the tip element and the equivalent coefficient equals to 0.7581. In the paper of Shi et al. (2014), the constant 1 was used for the triangular elements. However, we can find in their results that the numerically calculated displacement at the fracture tip (1.1016) is greater than the analytical solution (0.9758) with coefficient close to 0.88. As can be seen in our later calculations, using the value of 0.806, the calculated stress intensity factors can match with the analytical solutions well for inclined cracks. A more rigorous choice of the constant will be investigated in our future work.

The direction θ_0 in which the principal stress is maximized should satisfy the following conditions:

$$\frac{\partial\sigma_1}{\partial\theta}|_{\theta=\theta_0} = 0, \qquad \frac{\partial^2\sigma_1}{\partial^2\theta}|_{\theta=\theta_0} < 0 \tag{14}$$

Since the out-of-plane propagation (mode III fracture) is not considered in this paper, the twisting angle φ_0 (Fig. 5) is assumed to be 0. The search for kinking angle θ_0 is realized with the dichotomy which can find the target value quite efficiently.

After the growth direction is determined, the equivalent stress intensity factor K_{eq} presented by Schöllmann et al. (2002) for mixed-mode fracture propagation is used to judge when the propagation starts:

$$K_{eq} = \frac{1}{2}\cos\left(\frac{\theta_0}{2}\right)\left\{\begin{array}{l} K_I\cos^2\left(\frac{\theta_0}{2}\right) - \frac{3}{2}K_{II}\sin\left(\frac{\theta_0}{2}\right) + \\ \sqrt{\left[K_I\cos^2\left(\frac{\theta_0}{2}\right) - \frac{3}{2}K_{II}\sin\left(\frac{\theta_0}{2}\right)\right]^2 + 4K_{III}^2} \end{array}\right\} \tag{15}$$

The fracture growth rate is calculated with the following relations (Lazarus, 2003),

$$\Delta d = \Delta d_{\max}\left(\frac{K_{eq}}{K_{IC}}\right)^m \tag{16}$$

where$\Delta d_{max}$is the user-defined maximum propagation distance in a single step and$K_{IC}$is the mode-I fracture toughness. Currently, the fracture toughness is assumed to be constant during the fracturing process. However, the loading rate or loading strain may change the magnitude of fracture toughness in gas shales (Mahanta et al., 2017). Thus, the dynamic change of mechanical properties should also be considered if further improvement of model reliability is expected.

Generally, hydraulic fracture propagation is assumed to be quasi-static, that the maximum equivalent stress intensity factor $K_{eq}^{\max}$ should be equal toK_{IC} at every time step. To simulate the propagation of hydraulic fractures driven by injected fluid, an iterative algorithm is developed in our model to automatically adjust the injection pressure and

Table 2
Number of integration points required to satisfy the error tolerance.

Ratio: a/b	1	1.5	2	2.5	3	3.5	4	5
1D Gaussian points	6 × 3	9 × 3	12 × 3	15 × 3	17 × 3	20 × 3	23 × 3	39 × 3

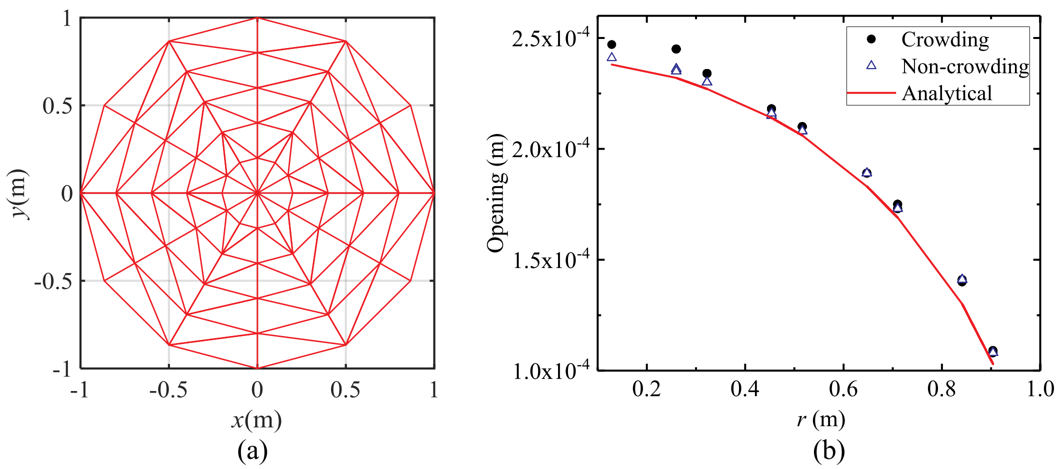

Fig. 4. (a) Triangular grid of the radial fracture with 108 elements; and (b) Comparison of fracture opening between numerical and analytical solutions with different choices of integration points (with the same number of 36).

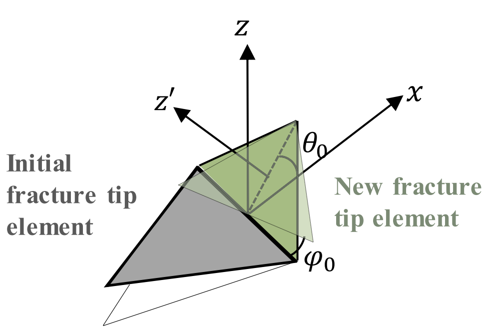

Fig. 5. Schematic of fracture tip coordinates and propagation directions.

time steps such that the mass balance condition and the quasi-static propagation assumption are simultaneously satisfied (Fig. 6). This routine contains two loops: the inner loop is for injection pressure determination, and the outer loop is used for time step calculation. The mass balance requirement can be met by adjusting the injection pressure, and the quasi-static propagation condition is satisfied by changing the time steps. In this model, the quasi-static propagation condition is defined such that the maximum equivalent stress intensity factor at current time step n is within the range of [(1-α, 1+α)], where$\alpha$is a small constant close to 0 and is taken to be 0.1 in this paper. The dichotomy is used to update both the injection pressure and time step length.

For the triangular element based DDM, the propagation vector with lengthΔd and angle θ_0 originates from the center of the front edge. The mesh growth method used by Meng et al. (2013) (Fig. 7(a)) connects the ends of all propagation vectors to construct the new fracture front and these ends become the vertexes of the new front elements. This strategy is reasonable when the propagation velocities of all fracture tips at each time step are approximately the same. Otherwise, the new fracture front can be zigzagged and the element will be distorted. To optimize the fracture geometries, a new mesh growth routine is proposed here (Fig. 7(b)).

As demonstrated in Fig. 7(b), the new fracture front is firstly smoothed using the 3rd order Savitzky-Golay filter (Savitzky and Golay, 1964) to eliminate obvious outliers. Then a new propagation vector originated from the tip element's vertex is reconstructed with the propagating direction being closely perpendicular to the old front by equally dividing the angle between the connected edges. Then, new fracture elements are added with three types of operations including splitting, merging and extending to optimize the element's geometric quality, as illustrated in Fig. 8.

The splitting operation is conducted when the length of the propagation vectorΔd is significantly smaller than the length of the element edgeL_{new}(Fig. 8(a)). To avoid the skewness of element, a new vertex will be added on the new edge to subdivide the element. For the case when two vector ends become quite close, the merging operation is used to merge the two ends into one (Fig. 8(b)). The extending operation is specially designed for stopping fracture front. If the growth rate of the element is quite slow, there is no need to add extremely small elements to rebuild the new fracture front. An extension of the current tip element can describe the new front effectively as well as reducing the computation cost (Fig. 8(c)). To avoid over stretching of the tip elements, a re-splitting operation is also implemented (Figs. 8(c-2)). The criteria used in this paper to trigger the above operations are defined as:

$$\begin{cases} splitting, & \Delta d \ < 0.5L_{new} \\ merging, & L_{new} < 0.5\Delta d \\ extending, & \Delta d \ < 0.3\Delta d_{\max} \end{cases} \quad (17)$$

Here, three examples are provided to illustrate the effectiveness of our model to capture complex fracture geometries (Fig. 9). All fractures are assumed to be perpendicular to the minimum horizontal stress and propagating in a homogeneous stress field thus no deflection would occur. As shown in Fig. 9(a), a fracture propagating radially is observed when the minimum horizontal stress distributes homogeneously. If stress barriers exist along the vertical direction, the growth of fracture height will be impeded, resulting in the shrinkage of grid size. When the stress barriers are penetrated, the grids in vertical direction are expanded again, representing the acceleration of height growth (Fig. 9(b)). However, if strong stress bounds are applied above and below the perforation layer, the growth of fracture height will stop and a PKN-shaped fracture is formed (Fig. 9(c)). Through the adaptive deformation of grid shapes, we're able to build a robust fracture propagation model to properly predict the fracture geometries under complex and heterogeneous stress conditions.

3. Results and discussions

3.1. Model validation

The calculation of stresses induced by fracture deformation and stress intensity factors (SIFs) will be validated first. Based on the theory of linear elastic fracture mechanics (LEFM), the normal stress induced by a pressurized radial fracture near the fracture tip satisfies the

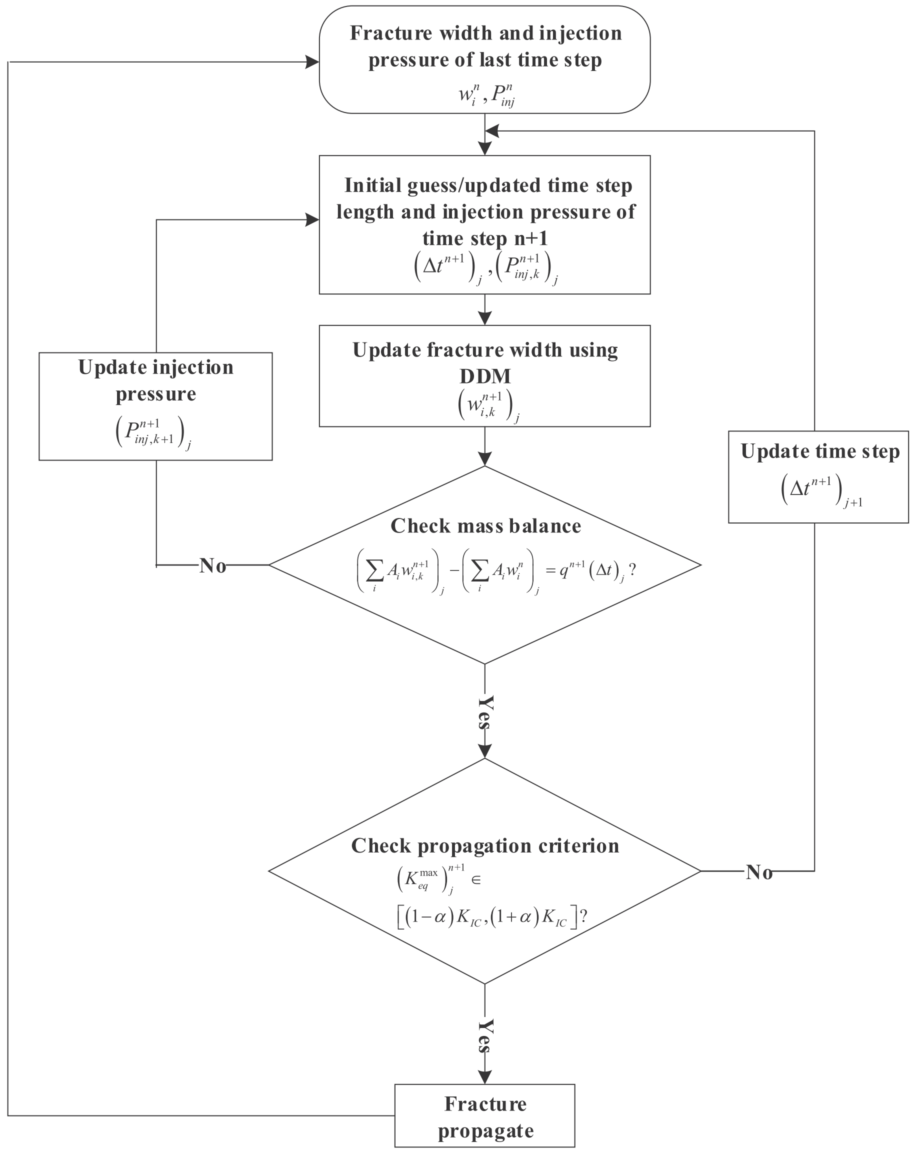

Fig. 6. Schematics of the fracture propagation algorithm (grid, injection pressure iteration and time step iteration are numbered with subscript i, k, j, respectively. Time step is denoted with superscript n and q is the volumetric injection rate).

following expressions (Sneddon 1946):

$$\sigma_n = -\frac{2p_0}{\pi}\left(\sin^{-1}\frac{1}{x-c} - \frac{1}{\sqrt{(x-c)^2-1}}\right) \tag{18}$$

where x is the radial distance between the source point and fracture center. Same grid with Fig. 4(a) is used and the net pressure (fluid pressure minus the *in-situ* normal stress) is assumed to be 2 MPa. The rock mechanical properties of Jiaoshiba gas shale reservoir listed in Table 3 (Xiao et al., 2016) are used for case studies, where the elastic properties (i.e. Young's Modulus, Poisson's Ratio) are measure with the

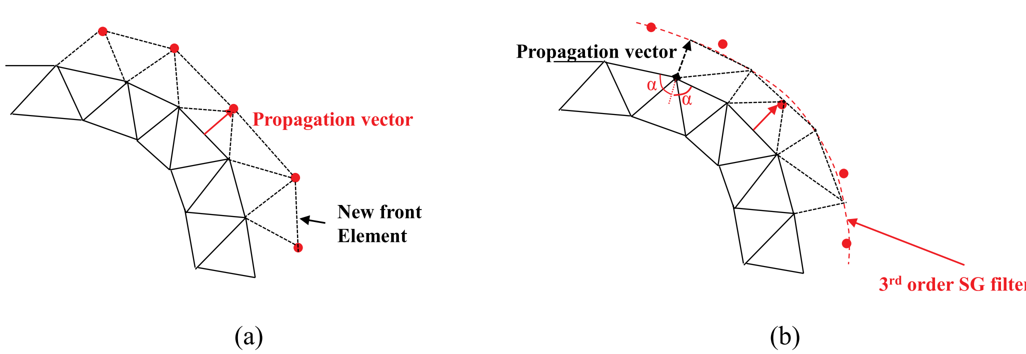

Fig. 7. Fracture mesh growth proposed by (a) Meng et al. (2013) and (b) this paper.

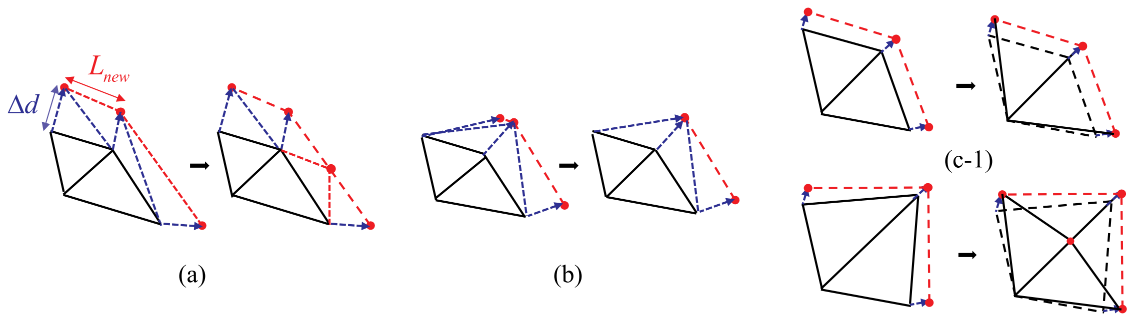

Fig. 8. Schematics of (a) splitting, (b) merging and (c) extending operations: (c-1) direct extending; (c-2) extending with re-splitting.

tri-axial compressional experiments under field conditions, fracture toughness is obtained with the three-point bending experiments and the typical fluid injection rate is taken from the field treatment data.

Fig. 10(a) shows that the numerical results match well with the analytical solutions, except a slight diversion at the locations that are very close to the tip. According to our observations from hundreds of simulations with a broad range of parameters, when the distance between the source point and fracture tip is within 1/2 length of element size, the numerically evaluated stresses can be significantly larger than the theoretical solutions. The accuracy of near-tip stress calculation can be improved with the utilization of nearly-singular integral calculation technologies (Johnston et al., 2013) which will not be further discussed here.

Validation of the stress intensity factor of a slanted fracture under pure tensile load is also presented. The analytical solutions of SIFs around an inclined pressurized penny-shaped fracture can be found in (Aliabadi, 2002) as:

$$K_I = \frac{2}{\pi}\sigma \cos^2 \phi\sqrt{\pi c}$$
$$K_{II} = \frac{4}{\pi(2-\nu)}\sigma \sin\phi \cos\phi \cos\omega\sqrt{\pi c}$$
$$K_{III} = \frac{4(1-\nu)}{\pi(2-\nu)}\sigma \sin\phi \cos\phi \sin\omega\sqrt{\pi c} \tag{19}$$

where $\sigma$is the applied tensile stress, the angle$\phi$and ω are defined in Fig. 11. Same mechanical properties and grid with the above case are used with applied tensile stress equals to 2 MPa. The simulation results of a slanted crack inclined at 30° is depicted in Fig. 10(b). As can be seen from this figure, a good agreement is obtained between our model and the analytical solutions.

The fracture propagation algorithm proposed in Fig. 6 is verified with the classical three-dimensional quasi-static evolution of a penny-shaped crack under Mode I conditions. Under the assumption of constant inner pressure, the net pressure and injected fluid volume required for radial fracture propagation follows (Abe et al., 1997):

Table 3
Input parameters for case studies.

Parameter	Unit	Value	Parameter	Unit	Value
Young's Modulus	GPa	35	Poisson's Ratio	–	0.23
Mode I toughness	MPa·(m)$^{1/2}$	1.2	Initial radius	m	10
Fluid injection rate	m^3/min	13	Δd_{max}	M	3
m	–	1	α	–	0.1

$$p(c) = K_{IC}\sqrt{\frac{\pi}{4c}}$$
$$V(c) = \frac{8}{3}\frac{K_{IC}}{E'}\sqrt{\pi c^5} \tag{20}$$

where $E' = E/(1\text{-}\nu^2)$. The material properties in Table 3 and fracture propagation routine in Fig. 6 are adopted. Fig. 12 shows the evolution of net pressure and fracture radius as a function of injected fluid volume. Also, a good match between numerical and analytical solutions can be achieved, which proves the reliability of our propagation strategies.

3.2. Stress interaction analysis for stationary fractures

The stress interactions among multiple stationary fractures with different geometries will be investigated in this section. Parameters listed in Table 3 are used.

Four sets of fractures, one set of radial fractures and three sets of PKN fractures are considered. The fractures in each set are equally spaced to represent three clusters in one fracturing stage. The radius of the radial fracture is 40 m, and the length and height of the PKN fractures are 100 m, 100 m, 200 m and 30 m, 60 m, 30 m respectively. All fractures are equally pressurized with net pressure 2 MPa. The opening of fractures with spacing 30m is calculated (Fig. 13). Note that, the color scale of each figure is different since the range of fracture width in each set is quite different. As can be seen from these figures, the inner fractures have smaller width compared to the outer fractures. The

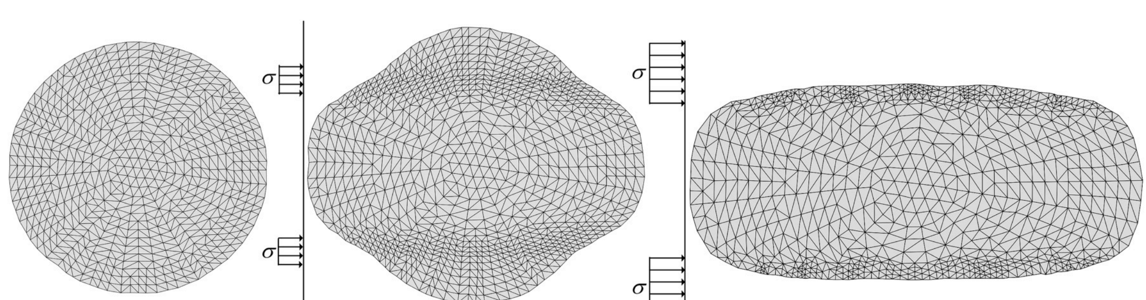

Fig. 9. Fracture propagation with different distribution of minimum horizontal stress: (a) homogeneous; (b) two stress barriers; (c) strong upper and lower stress bounds.

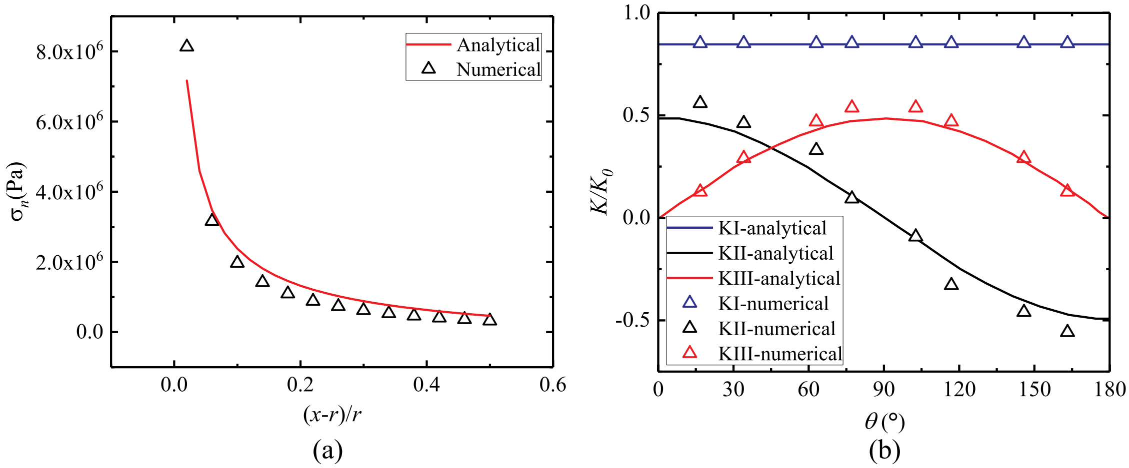

Fig. 10. (a) Comparison of near-tip normal stress between numerical and analytical solutions and (b) SIFs variation along the penny-shaped crack inclined at 30° of exact solution (solid line) and numerical solutions (triangle) ($K_0 = \sigma\sqrt{c}$).

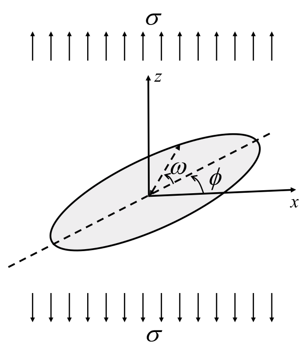

Fig. 11. Schematic of inclined radial fracture under tensile loading.

difference between middle and side fracture is largest for radial-shaped fractures because the radial fractures have the smallest averaged distance between each element (Fig. 13(a)). In addition, the larger the PKN fractures are, the stronger the stress shadowing effect is. For the PKN fractures, the strength of stress interaction is more sensitive to fracture height than fracture length as show in Fig. 13(b)–13(d).

The change of fracture width difference (the ratio of outer fracture central width to inner fracture central width) with cluster spacing is plotted on Fig. 14 with additional results calculated with 2D model (the black dashed line). As expected, the width difference decreases with the increasing spacing. In addition, the 2D model would over-estimate the stress interactions due to its infinite height assumption. It is clear in Fig. 14 that the difference of fracture openings does not change significantly when decreasing fracture length from 200 m to 100 m (from green curve to red curve), but a significant reduction of stress interactions can be observed when the fracture height becomes half of the original size (from blue curve to red curve). Thus, for PKN fractures, when designing the fracture spacing with consideration of mechanical interactions, the fracture height would be a more important factor to be considered than fracture length.

The stresses induced by three equally sized PKN fractures with $L = 200$ m, $H = 30$ m are also calculated. The distribution of stresses in x and y direction is shown in Fig. 15(a) and Fig. 15(b) (the sign convention is that tensile stress is positive). A region of greater compressional stress (color in blue) is observed between the fracture surfaces. In addition, the induced compressional stress along x direction (S_{xx}) is greater than stress S_{yy} which implies a potential stress reorientation zone close to the fractures. Fig. 15(c) draws the field of stress difference $dS = S_{xx} - S_{yy}$ and the regions of value below zero might experience stress reorientation due to the stress interference among fractures. The iso-surfaces in Fig. 15(d) show that the potential stress-reorientation regions extend further in the vertical and x directions than ahead of the fracture length. The areas where tensile stresses are induced (color in red) will enlarge the stress difference (regions around fracture tips), prohibiting stress-reorientation and the generation of complex fracture networks as analyzed in the literature (Gu and Weng, 2010).

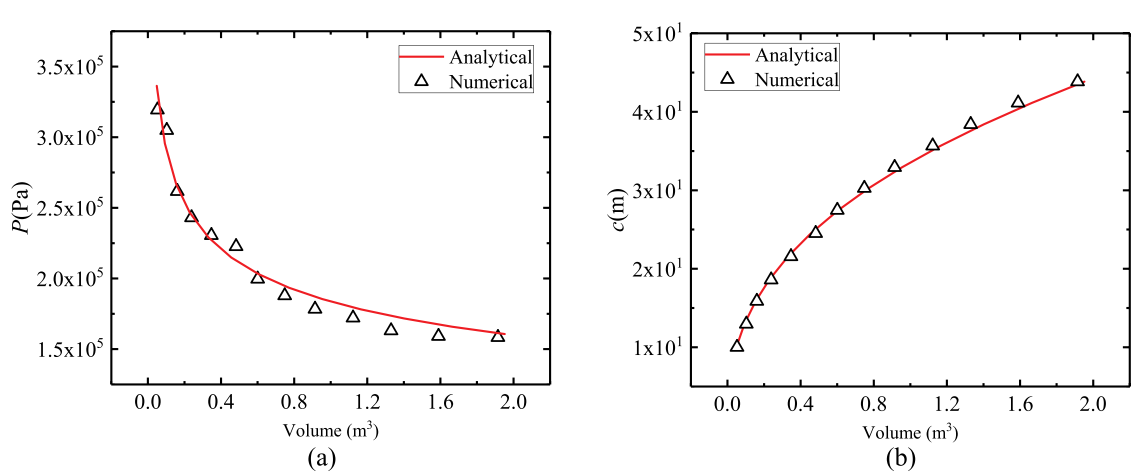

Fig. 12. Evolution of (a) net pressure and (b) radius of the crack as a function of the injected fluid volume.

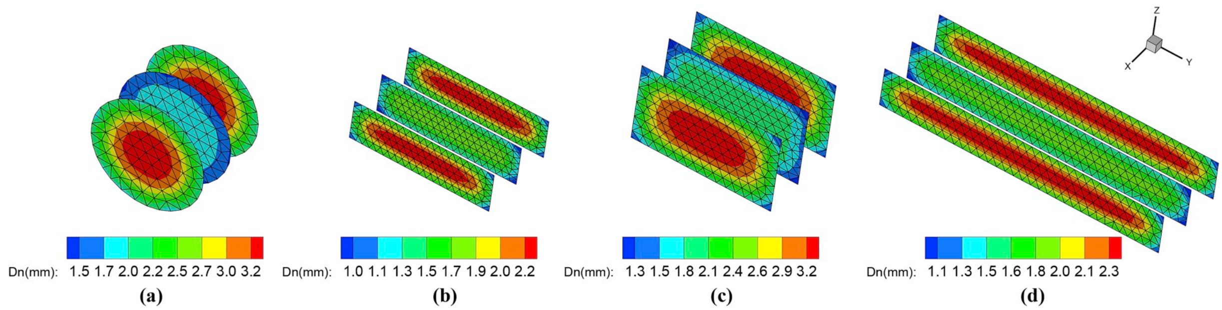

Fig. 13. Fracture opening of (a) 3 radial fractures with radius of 40m, (b) 3 PKN fractures with $H = 30$ m, $L = 100$ m, (c) PKN fracture with $H = 60$ m, $L = 100$ m, and (d)PKN fractures with $H = 30$ m, $L = 200$ m when fracture space equals to 30 m.

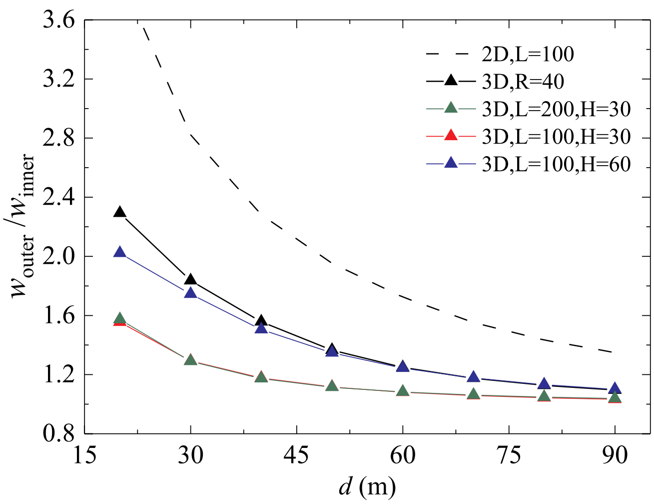

Fig. 14. The relation between fracture spacing d and width ratio between outer and inner fractures.

3.3. Multiple fracture propagation

The above section has analyzed the influence of mechanical interactions among multiple stationary hydraulic fractures on fracture opening and stress redistribution. In fact, not only the opening, but also the shape of fractures could be affected. The impact of fracture spacing, stress heterogeneity and fracture inclination on multiple propagating hydraulic fractures are going to be investigated in this section. The input parameters for the following cases are provided in Table 3 and the injection time is 15 s in total (If the pressure loss caused by fluid viscosity is considered, longer injection time will be required for fractures to propagate the same distance).

In the first case, the role of fracture spacing in multiple fracture propagation is analyzed. The initial fractures are assumed to be radial with radius equals to 10 m. The *in-situ* stresses in x, y and z directions are homogeneous in the whole domain with constant value 20 MPa. The crack surfaces after injecting fluid for 15 s are shown in Fig. 16(a) and Fig. 16(b) with spacing 30 m and 10 m, respectively. The curving of outer fractures and the growth prohibition of inner fractures are clearly observed. As the fractures approach, strong curving occurs and the growth of the inner fracture gets harder. The side fractures are pushed away from the central part by the induced stresses, resulting in bowl-shaped geometry which has been observed in the thermal shock experiments (Fig. 16(c)) (Wu et al., 2016). The impact of fracture spacing can be seen more quantitatively in Fig. 18. With the decrease of fracture space, smaller amount of injecting fluid enters the middle fracture (Fig. 18(a)), resulting in greater difference in fracture surface area between the inner and outer fractures (Fig. 18(b)).

The changes of fracture shape with vertical *in-situ* stress heterogeneity are shown in Fig. 17. Different from the homogeneous cases, strong and weak stress barriers exist for the cases in Fig. 17(a) and (b) respectively. In the stress barriers, the *in-situ* stresses in all directions are increased with the same value. Since the propagation in vertical direction is limited by these barriers, the fracture length starts to grow faster than the height. In Fig. 17(a), all fractures are contained in the perforation layer and the resultant geometries are PKN-shaped. If the stress barriers are weak, there is a chance for the fractures to penetrate the high stress layers and regain the ability of height growth as shown in Fig. 17(b). Comparing Figs. 17 and 18, we can find that the fracture opening difference in homogeneous *in-situ* stress field is greater than the height contained cases, which is consistent with the conclusions drawn for stationary fractures.

As shown in Fig. 18, before crossing the stress barriers, the fluid partitioning and surface area evolution of the multi-layered case in Fig. 18(b) (empty triangles) is quite close to the PKN-shaped fractures in Fig. 18(a) (dashed dot lines). However, after breaking through the stress constraints, the effect of stress barriers on fracture propagation vanishes and the behaviors of fractures become more similar with the radial cases in Fig. 18(a) (solid lines). In addition, as shown in Fig. 18, the fractures propagating in homogeneous *in-situ* stress field experience the strongest unbalance distribution of injection fluid and growth of hydraulic fractures while the PKN-shaped fractures have the most evenly distribution of both fluid and fracture surface area. The above four cases highlight the importance of vertical heterogeneity of *in-situ* stresses on fracture propagation and interactions. In the following part, we will discuss a more complex situation.

One advantage of the 3D model is its capacity to describe strong curving of hydraulic fractures in the near well regions when the initial mini-fracture is not perpendicular to the minimum horizontal stress. The following case is designed to show how the fracture will propagate when the normal direction of initial fracture plane deviates from x axis under complex stress states as shown in Fig. 20(a) ~ (d). An inclination angle of 30° is preset and same as above, the fractures are equally spaced with 30 m (Fig. 19(a)).

In the previous cases, the *in-situ* stresses in all directions are the same in each layer. However, in reality, the variation of each principal stress may be different vertically for the reasons such as the change of rock properties and tectonic strains. In the following case, we assume the increase of over-burden stress is faster than the other principal stresses (Fig. 19). The stress regimes change from reverse ($\sigma_{zz} < \sigma_{xx} < \sigma_{yy}$) to normal ($\sigma_{xx} < \sigma_{yy} < \sigma_{zz}$) along the vertical depth h.

Fig. 20 shows the evolution of fracture geometry and opening distribution with time. As the fractures start to propagate, the fracture surfaces turn and propagate from the initial plane to be perpendicular to the minimum horizontal stress (Fig. 20(b)), as described in the literature (Yew, 2007). Once entering layers L2 and L4, the growth of fracture height slows down due to the greater *in-situ* stresses in-place (Fig. 20(c)). The fracture surfaces tend to bend to be parallel to the horizontal plane since the minimum principal stress becomes vertical in this zone. On the other hand, for the downward moving fracture parts,

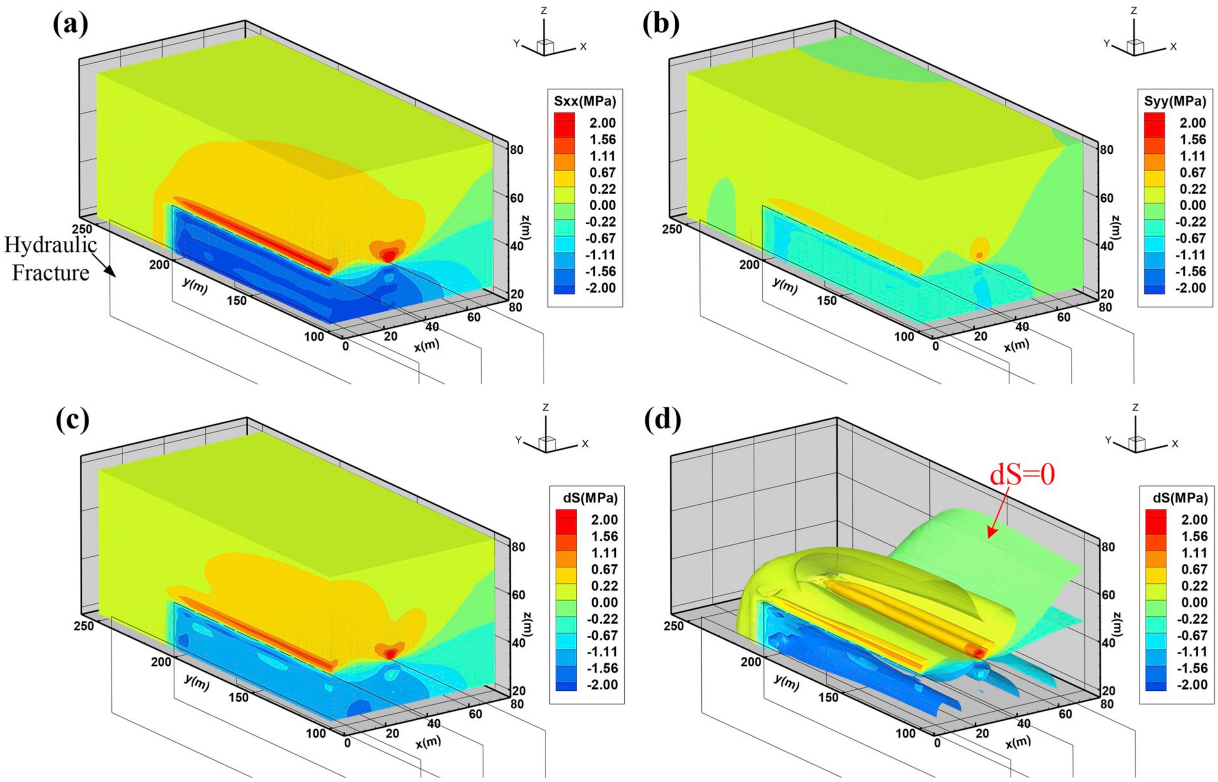

Fig. 15. Stress fields: (a) S_{xx}, (b) S_{yy}, (c) dS = (S_{xx}-S_{yy}) and (d) iso-surfaces of dS induced by three PKN fractures (L = 200 m, H = 30 m). In consideration of symmetry, only 1/8 region is displayed (theses rectangle frames represent the hydraulic fractures).

they tend to rotate perpendicular to x direction when entering the normal stress regime (Fig. 20(d)). What's more, the initial fracture planes are obviously narrower compared to their surroundings because of the greater normal stress applied, which could potentially result in proppant bridging in the near well regions. The purpose of this case is to demonstrate the significance of three *in-situ* principal stresses compared to the often discussed two horizontal stresses in predicting fracture propagation. With the consideration of all three *in-situ* stresses, a more accurate and comprehensive understanding of fracture geometry can be achieved.

4. Conclusions

In this study, a three-dimensional displacement discontinuity program based on the theory of LEFM, is developed and employed for stress and fracture propagation analysis. The numerical solutions for singular and non-singular integrals in influence coefficients on triangular elements are systematically introduced. Optimization strategies, such as non-crowding and distance-dependent integrals, adaptive grid adjustment operations, are proposed to improve the model accuracy and efficiency. Numerical simulations of mechanical interactions of closely spaced hydraulic fractures using this model concluded the

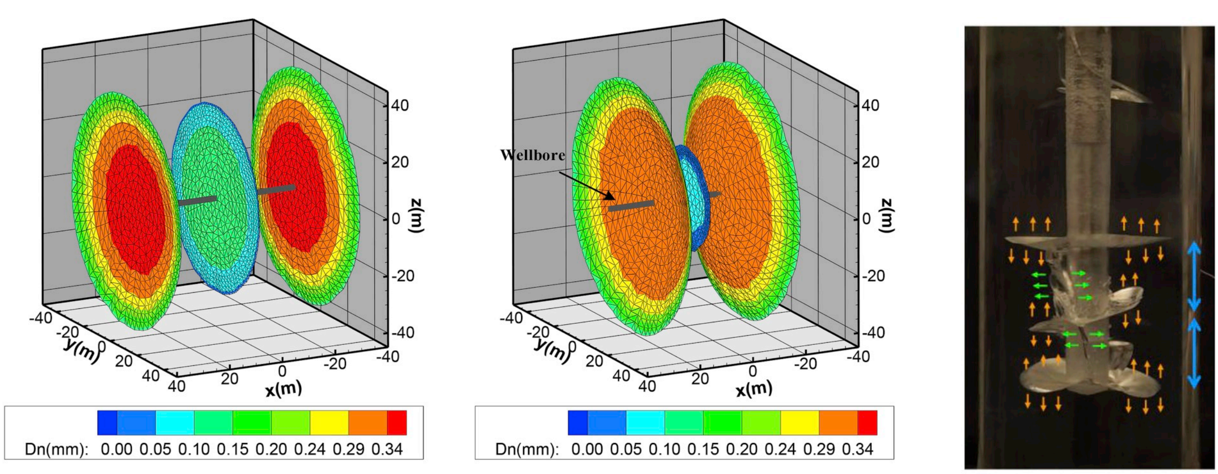

(a) (b) (c)

Fig. 16. Geometries of hydraulic fractures with spacing (a) 30 m and (b) 10 m in homogeneous *in-situ* stress field after injection for 15 s and (c) is the morphology of cracks generated from cryogenic thermal shock at the borehole geometry (Wu et al., 2016) (green arrows: vertical circumferential tensile crack due to circumferential thermal contraction; orange arrows: horizontal radial planar cracks caused from longitudinal thermal contraction; blue arrows: exclusion distance). (For interpretation of the references to color in this figure legend, the reader is referred to the Web version of this article.)

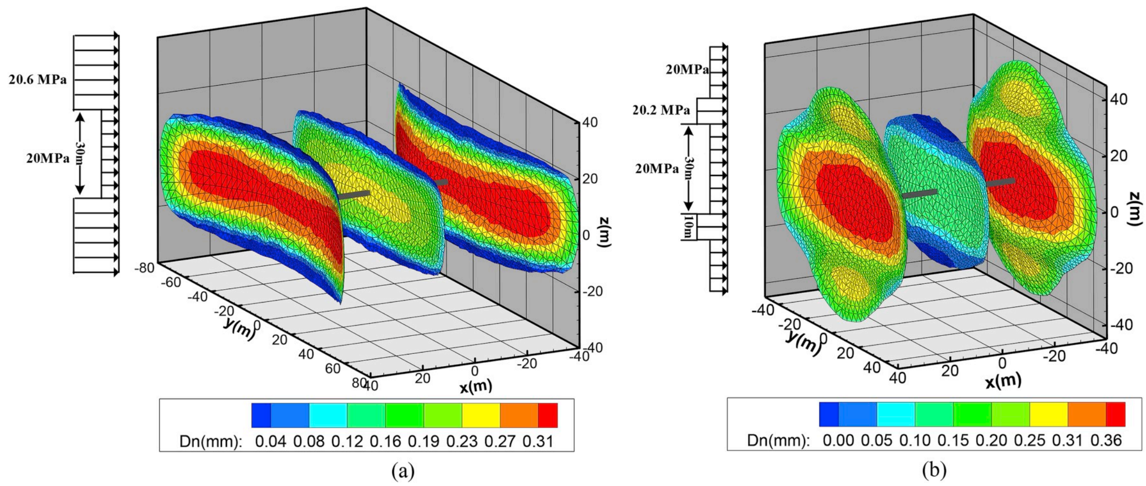

Fig. 17. Distribution of fracture opening for the case of (a) strong (b) weak stress barriers.

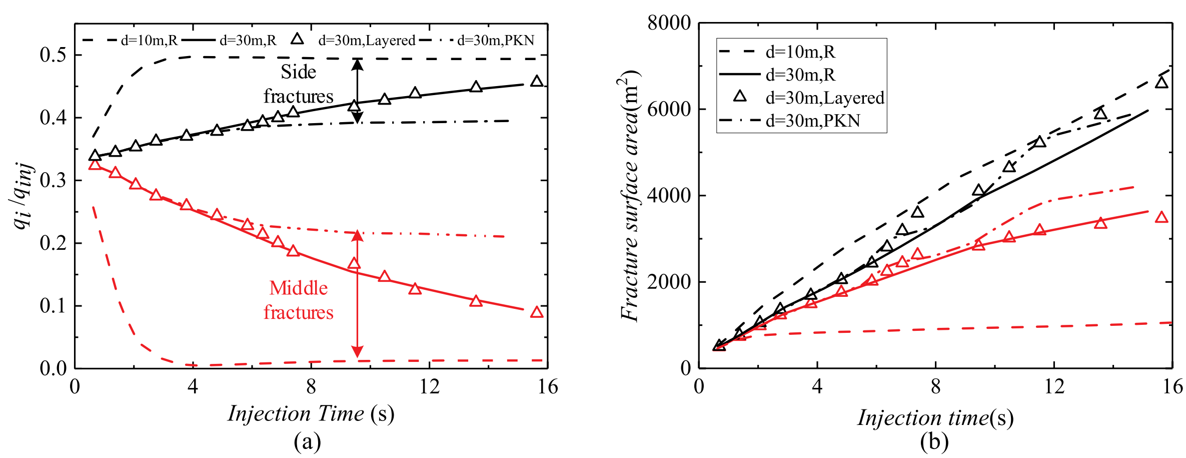

Fig. 18. Comparison of the evolution of (a) injecting fluid partitioning and (b) half fracture surface area with injection time for the cases in Fig. 17 and 18 (*d* represents the fracture spacing, 'R' represents radial fractures, 'Layered' denotes the case in Figure18(b) with multiple stress layers and PKN corresponds to the fracture geometry in Figure18(a)).

following remarks:

1. The strength of stress interference not only depends on the cluster spacing, but also on the fracture shapes. According to the 3D simulations, the shorter edge of PKN fracture dominates the stress shadowing effect and the radial fractures experience the strongest interactions compared to other fracture shapes.
2. A reasonable evaluation of fracture induced stresses can be achieved with the proposed model and the potential stress-reorientation regions in three-dimensional space is much more complex than 2D.
3. The geometry of multiple propagating hydraulic fractures is significantly affected by the *in-situ* stress layers. The limitation on fracture height growth can reduce the mechanical interactions due to the decrease of induced opening and stresses.
4. Fracture curving due to near-well tortuosity can also be effectively modelled with our model. In such situations, all three *in-situ* stresses

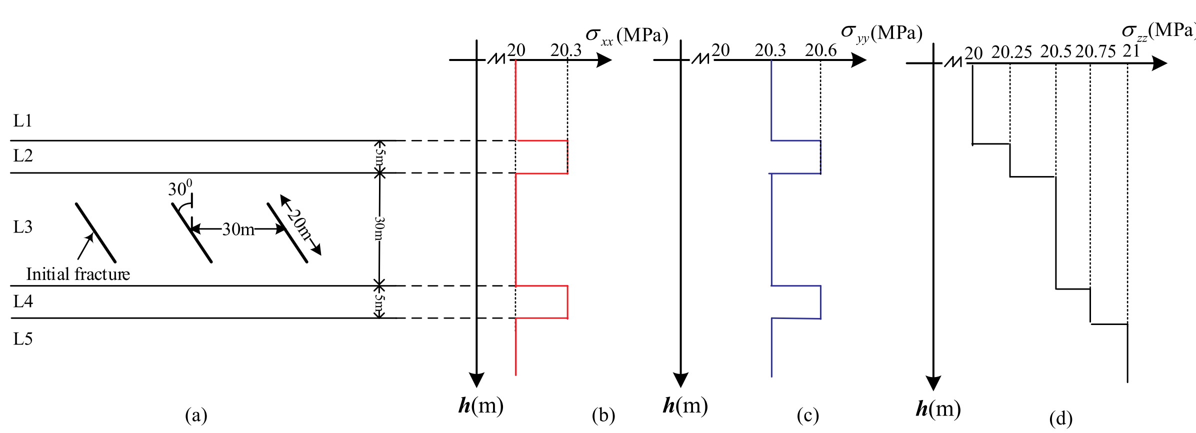

Fig. 19. (a) Schematics of stress layers (Li, i = 1,2,..,5) and initial fractures; (b)–(d) Distribution of *in-situ* stress σ_{xx}, σ_{yy} and σ_{zz} in each layer respectively.

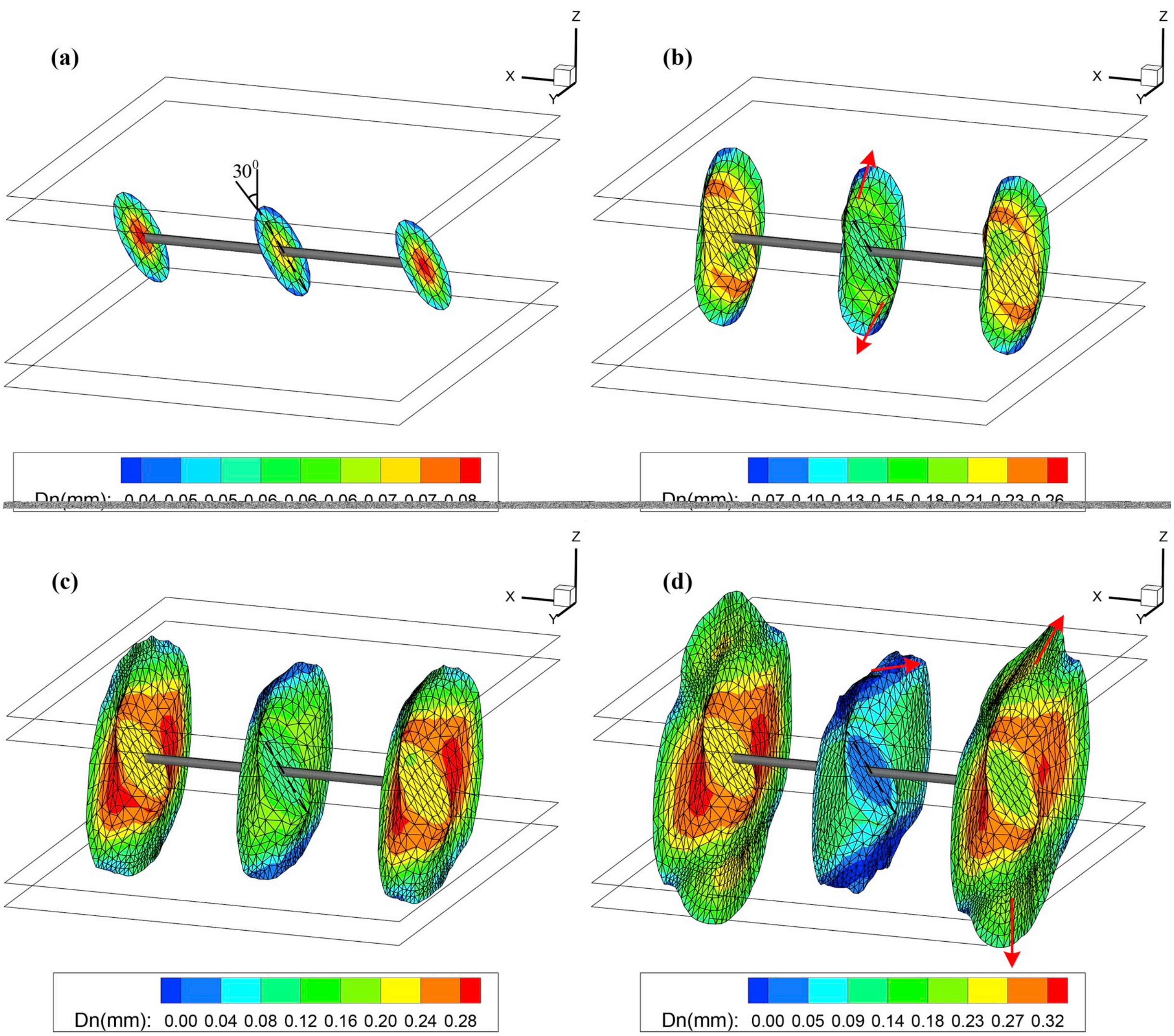

Fig. 20. Evolution of fracture geometry and opening with inclined initial surfaces in *in-situ* stress field Fig. 20(b) at time (a) 2.5 s, (b) 3.2 s, (c) 5.9 s and (d)10 s respectively. The red arrows highlight the current growth trend of fracture fronts. (For interpretation of the references to color in this figure legend, the reader is referred to the Web version of this article.)

should be carefully considered to deliver proper prediction of fracture geometries.

The numerical model proposed in this paper is capable of treating strong heterogeneity of *in-situ* stresses by its self-adjustment in grid shapes. This model can be used to predict the complexity of hydraulic fractures in the vicinity of wellbores since curving propagation of fractures in real 3D space is considered reasonably and the corresponding stress perturbation and evolution can be captured accurately. Thus, it can serve as a useful tool for the optimization of perforation

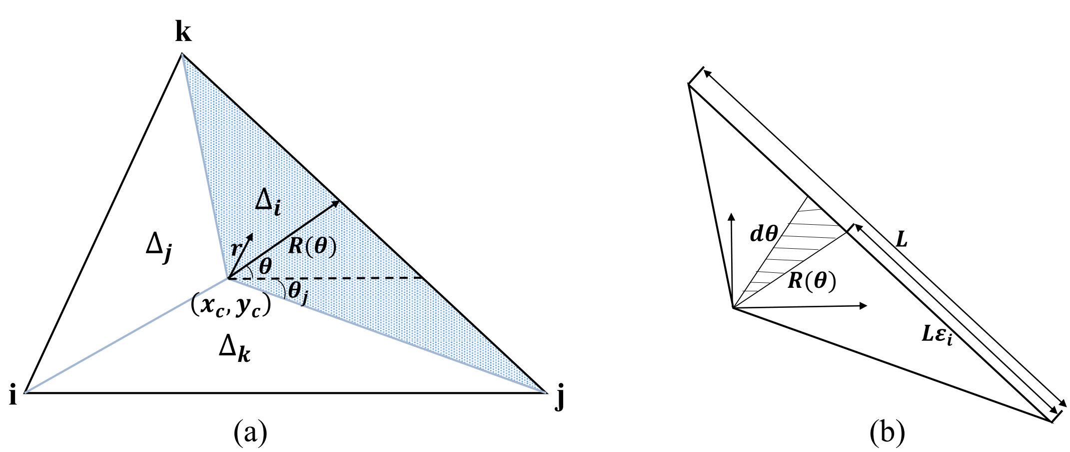

Fig. 21. (a)Schematics of triangle subdivision and multiple coordinate systems; (b)Transformation between radial and areal coordinates.

design. The conclusions drawn above are based on the assumption of constant net pressure in each time step which will be more reliable when more mechanisms are considered. Currently, only mechanical part is included in this model. The fluid flow in wellbores, hydraulic fractures and transport of proppant have been considered in our Planar-3D models (Tang et al., 2016) and will be added in the fully 3D framework in a future work. Though the efficiency of the fully 3D model can be improved with the methods suggested in this paper, its cost in storage and computing time is still much more than the lower dimensional models. A proper choice of model dimension requires comprehensive comparison and understanding of the limitations of each model which also needs to be aided by the fully 3D models.

Acknowledgments

The authors would like to thank Dr. Kinpang Cheong for his valuable and helpful comments on this paper. This work was supported by the National Natural Science Foundation of China (Grant No. 51874251), Open foundation of State Key Laboratory of Oil and Gas Reservoir Geology and Exploitation (Southwest Petroleum University) (Grant No. PLM201819) and Sichuan Science and Technology Program (Grant No. 2019JDRC0089)

Appendix A. Supplementary data

Supplementary data to this article can be found online at https://doi.org/10.1016/j.petrol.2019.04.050.

APPENDIX A. Calculation of singular integrals in influence coefficients

The integral of a third order derivative $I_{,xxx}$ in Eq. (2) reads:

$$I_{,xxx}=\iint\limits_{\Delta}\frac{-15(x-\xi)^3}{[(x-\xi)^2+(y-\eta)^2+z^2]^{7/2}}+\frac{9(x-\xi)}{[(x-\xi)^2+(y-\eta)^2+z^2]^{5/2}}d\xi d\eta. \tag{A.1}$$

When the source point x,y,z is located in the cell center, i.e.$x=x_c$, $y=y_c$, $z=0$, a polar coordinate transformation centered at the source point is applied first (Fig. 21),

$$\begin{aligned}\xi&=x_c+r\cos\theta\\ \eta&=y_c+r\cos\theta\end{aligned} \tag{A.2}$$

The integral then becomes,

$$I_{,xxx}=\iint\limits_{\Delta}\left[\frac{-15(-r\cos\theta)^3}{r^7}+\frac{9(-r\cos\theta)}{r^5}\right]rd\theta dr=\iint\limits_{\Delta}\frac{15(\cos\theta)^3-9\cos\theta}{r^3}d\theta dr. \tag{A.3}$$

which is of third order of singularity. Though the polar transformation has already reduced the order by one, this transformed integral still cannot be solved with regular integration methods. A subdivision of the triangular element is applied before further calculations.

As displayed in Fig. 21(a), originating from the gravity center, the triangle *ijk* is divided into three sub-regionsΔ_i, $\Delta_j$andΔ_k. The integral over the whole domain becomes a summation of the integrals in each small triangle and the integral on$\Delta_i$can be written as:

$$\begin{aligned}&(I_{,xxx})_{\Delta_i}\\ &=\iint\limits_{\Delta_i}\frac{15(\cos\theta)^3-9\cos\theta}{r^3}drd\theta=\int\limits_{\theta_j}^{\theta_k}[15(\cos\theta)^3-9\cos\theta]d\theta\int\limits_0^{R(\theta)}\frac{1}{r^3}dr.\end{aligned} \tag{A.4}$$

The hyper singular part $\int\limits_0^{R(\theta)}(1/r^3)dr$ can be obtained in the sense of Hadamard's finite part with:

$$F.\ P.\int\limits_0^{R(\theta)}\frac{1}{r^3}dr=\frac{1}{2R(\theta)}. \tag{A.5}$$

Then the integrals are transformed from the polar coordinates to areal coordinates as shown in Fig. 21(b):

$$d\theta=\frac{2A_i}{R^2(\theta)}d\varepsilon_i. \tag{A.6}$$

The rest variables in Eq. (A.4) are transformed into

$$\begin{aligned}&\sin\theta=\frac{y_m^{\prime\prime}}{R(\theta)},\ \cos\theta=\frac{x_m^{\prime\prime}}{R(\theta)},\ R(\theta)=\sqrt{x_m^{\prime\prime2}+y_m^{\prime\prime2}},\\ &x_m^{\prime\prime}=(1-\varepsilon_i)x_j^{\prime\prime}+\varepsilon_i x_k^{\prime\prime},\quad y_m^{\prime\prime}=(1-\varepsilon_i)y_j^{\prime\prime}+\varepsilon_i y_k^{\prime\prime}\end{aligned} \tag{A.7}$$

in the new coordinate system.

Taking Eqs. (A.5)-(A.7) into Eq. (A.3), we can get

$$\begin{aligned}(I_{,xxx})_{\Delta_i}&=2A_i\int\limits_0^1\frac{15(\cos\theta)^3-9\cos\theta}{2R^3(\theta)}d\varepsilon_i=2A_i\int\limits_0^1\left(\frac{15x_m^{\prime\prime3}}{2R(\theta)^6}-\frac{9x_m^{\prime\prime}}{2R(\theta)^4}\right)d\varepsilon_i\\ &=2A_i\int\limits_0^1 g(\varepsilon_i)d\varepsilon_i\end{aligned} \tag{A.8}$$

where A_i is the area of the sub-triangleΔ_i. At this point, all integrals in the presented methodology are regular, which can be evaluated accurately and efficiently using one dimensional Gaussian integrals. This routine can also been used for strongly and weakly singular integrals with changes in$g(\varepsilon_i)$. The expressions of $g(\varepsilon_i)$ for each integral is shown below:

The derivative of kernel function I can be written as:

$$I_{,ij} = \iint_{\Delta} i_{,ij} d\xi d\eta, \qquad i, j = x, y, z$$
$$I_{,ijk} = \iint_{\Delta} i_{,ijk} d\xi d\eta, \qquad i, j, k = x, y, z \tag{A.9}$$

where the items to be integrated in Eq (A.9) are:

$$\begin{aligned}
i_{,xx} &= \frac{3(x-\xi)^2}{r^5} - \frac{1}{r^3}, \qquad i_{,yy} = \frac{3(y-\eta)^2}{r^5} - \frac{1}{r^3}\\
i_{,zz} &= \frac{3z^2}{r^5} - \frac{1}{r^3}, \qquad i_{,xy} = \frac{3(x-\xi)(y-\eta)}{r^5}\\
i_{,xz} &= \frac{3(x-\xi)z}{r^5}, \qquad i_{,yz} = \frac{3(y-\eta)z}{r^5}\\
i_{,xxx} &= \frac{-15(x-\xi)^3}{r^7} + \frac{9(x-\xi)}{r^5}\\
i_{,yyy} &= \frac{-15(y-\eta)^3}{r^7} + \frac{9(y-\eta)}{r^5}\\
i_{,zzz} &= \frac{-15z^3}{r^7} + \frac{9z}{r^5}\\
i_{,xxy} &= \frac{-15(x-\xi)^2(y-\eta)}{r^7} + \frac{3(y-\eta)}{r^5}\\
i_{,xxz} &= \frac{-15(x-\xi)^2 z}{r^7} + \frac{3z}{r^5}\\
i_{,yyz} &= \frac{-15(y-\eta)^2 z}{r^7} + \frac{3z}{r^5}\\
i_{,xyy} &= \frac{-15(y-\eta)^2(x-\xi)}{r^7} + \frac{3(x-\xi)}{r^5}\\
i_{,xyz} &= \frac{-15(x-\xi)(y-\eta)z}{r^7}\\
i_{,xzz} &= \frac{-15(x-\xi)z^2}{r^7} + \frac{3(x-\xi)}{r^5}\\
i_{,yzz} &= \frac{-15(y-\eta)z^2}{r^7} + \frac{3(y-\eta)}{r^5}
\end{aligned} \tag{A.10}$$

where

$$r = [(x-\xi)^2 + (y-\eta)^2 + z^2]^{1/2}$$

The expressions of integrated singular parts in the sense of Hadamard's finite part after coordinate transformation can be written as in Eq (A.11). The expressions of $x_m^{\prime\prime}$, $y_m^{\prime\prime}$ and $R(\theta)$ can be found in the main text and A_i is the area of sub-triangle i.

$$\begin{aligned}
F.\,P.\iint_{A_i} \frac{1}{r^3} dA &= -2A_i \int_0^1 \frac{1}{R^3(\theta)} d\varepsilon_k\\
F.\,P.\iint_{A_i} \frac{(x-\xi)^2}{r^5} dA &= -2A_i \int_0^1 \frac{x_m^{\prime\prime 2}}{R^5(\theta)} d\varepsilon_k\\
F.\,P.\iint_{A_i} \frac{(x-\xi)(y-\eta)}{r^5} dA &= -2A_i \int_0^1 \frac{x_m^{\prime\prime} y_m^{\prime\prime}}{R^5(\theta)} d\varepsilon_k\\
F.\,P.\iint_{A_i} \frac{(x-\xi)^3}{r^7} dA &= -A_i \int_0^1 \frac{x_m^{\prime\prime 3}}{R^6(\theta)} d\varepsilon_k\\
F.\,P.\iint_{A_i} \frac{(x-\xi)}{r^5} dA &= -A_i \int_0^1 \frac{x_m^{\prime\prime}}{R^4(\theta)} d\varepsilon_k\\
F.\,P.\iint_{A_i} \frac{(x-\xi)^2(y-\eta)}{r^7} dA &= -A_i \int_0^1 \frac{x_m^{\prime\prime 2} y_m^{\prime\prime}}{R^6(\theta)} d\varepsilon_k
\end{aligned} \tag{A.11}$$

Then, the singular integrals in each sub-triangle can be calculated according to Eq. (A.8).

References

Abass, H.H., Hedayati, S., Meadows, D.L., 1996. Nonplanar fracture propagation from a horizontal wellbore: experimental study. SPE Prod. Facil. 11 (03), 133–137. https://doi.org/10.2118/24823-PA.

Abe, H., Keer, L.M., Mura, T., 1997. Growth rate of a penny-shaped crack in hydraulic fracturing of rock. J. Geophys. Res. 81 (35), 6292–6298. https://doi.org/10.1029/JB081i035p06292.

Aliabadi, M.H., 2002. The Boundary Element Method, Applications in Solids and Structures. John Wiley & Sons.

Bunger, A.P., 2013. Analysis of the power input needed to propagate multiple hydraulic fractures. Int. J. Solids Struct. 50 (10), 1538–1549. https://doi.org/10.1016/j.ijsolstr.2013.01.004.

Bunger, A., Jeffrey, R.G., Zhang, X., 2014. Constraints on simultaneous growth of hydraulic fractures from multiple perforation clusters in horizontal wells. SPE J. 19 (04), 608–620. https://doi.org/10.2118/163860-PA.

Castonguay, S.T., Mear, M.E., Dean, R.H., 2013. Predictions of the growth of multiple interacting hydraulic fractures in three dimensions. In: SPE Annual Technical Conference and Exhibition, Society of Petroleum Engineers, https://doi.org/10.2118/166259-MS.

Cheng, Y., 2012. Mechanical interaction of multiple fractures–exploring impacts of the selection of the spacing/number of perforation clusters on horizontal shale-gas wells. SPE J. 17 (04), 992–1001. https://doi.org/10.2118/125769-PA.

Cheng, W., Jin, Y., Chen, M., 2015. Experimental study of step-displacement hydraulic fracturing on naturally fractured shale outcrops. J. Geophys. Eng. 12 (4), 714–723. https://doi.org/10.1088/1742-2132/12/4/714.

Cohen, C.E., Kresse, O., Weng, X., 2017. Stacked height model to improve fracture height growth prediction, and simulate interactions with multi-layer DFNs and ledges at weak zone interfaces. In: SPE Hydraulic Fracturing Technology Conference and Exhibition. Society of Petroleum Engineers. https://doi.org/10.2118/184876-MS.

Crouch, S.L., Starfield, A.M., Rizzo, F.J., 1983. Boundary element smethods in solid mechanics. J. Appl. Mech. 50, 704. https://doi.org/10.1115/1.3167130.

Dehghan, A.N., Goshtasbi, K., Ahangari, K., Jin, Y., Bahmani, A., 2017. 3D numerical

modeling of the propagation of hydraulic fracture at its intersection with natural (pre-existing) fracture. Rock Mech. Rock Eng. 50 (2), 367–386. https://doi.org/10.1007/s00.
Dohmen, T., Zhang, J., Blangy, J.P., 2014. Measurement and analysis of 3D stress shadowing related to the spacing of hydraulic fracturing in unconventional reservoirs. In: SPE Annual Technical Conference and Exhibition. Society of Petroleum Engineers. https://doi.org/10.2118/170924-MS.
Dontsov, E.V., Peirce, A.P., 2015. An enhanced pseudo-3D model for hydraulic fracturing accounting for viscous height growth, non-local elasticity, and lateral toughness. Eng. Fract. Mech. 142, 116–139. https://doi.org/10.1016/j.engfracmech.2015.05.043.
Geyer, J.F., Nemat-Nasser, S., 1982. Experimental investigation of thermally induced interacting cracks in brittle solids. Int. J. Solids Struct. 18 (4), 349–356. https://doi.org/10.1016/0020-7683(82)90059-2.
Gu, H., Weng, X., 2010. Criterion for fractures crossing frictional interfaces at non-orthogonal angles. In: 44th US Rock Mechanics Symposium and 5th US-Canada Rock Mechanics Symposium. American Rock Mechanics Association, > ARMA-10-198.
Guiggiani, M., Krishnasamy, G., Rudolphi, T.J., Rizzo, F.J., 1992. A general algorithm for the numerical solution of hypersingular boundary integral equations. J. Appl. Mech. 59 (3), 604–614.
Gupta, P., Duarte, C.A., 2018. Coupled hydromechanical-fracture simulations of nonplanar three-dimensional hydraulic fracture propagation. Int. J. Numer. Anal. Methods Geomech. 42 (1), 143–180. https://doi.org/10.1002/nag.2719.
Haddad, M., Sepehrnoori, K., 2016. XFEM-based CZM for the simulation of 3D multiple-cluster hydraulic fracturing in quasi-brittle shale formations. Rock Mech. Rock Eng. 49 (12), 4731–4748. https://doi.org/10.1007/s00603-016-1057-2.
Hussain, F., Karim, M.S., Ahamad, R., 2012. Appropriate Gaussian quadrature formulae for triangles. Int J Appl Math Comput 4 (1), 24–38. https://doi.org/10.0000/ijamc.2012.4.1.314.
Johnston, B.M., Johnston, P.R., Elliott, D., 2013. A new method for the numerical evaluation of nearly singular integrals on triangular elements in the 3D boundary element method. J. Comput. Appl. Math. 245, 148–161. https://doi.org/10.1016/j.cam.2012.12.018.
Kumar, D., Ghassemi, A., 2015. 3D simulation of multiple fracture propagation from horizontal wells. In: 49th US Rock Mechanics/Geomechanics Symposium, American Rock Mechanics Association, ARMA-2015-585.
Kuriyama, K., Mizuta, Y., 1993. Three-dimensional elastic analysis by the displacement discontinuity method with boundary division into triangular leaf elements. Int. J. Rock Mech. Min. Sci. 30 (02), 111–123. https://doi.org/10.1016/0148-9062(93)90704-H.
Lachat, J.C., Watson, J.O., 1976. Effective numerical treatment of boundary integral equations: a formulation for three-dimensional elastostatics. Int. J. Numer. Methods Eng. 10 (5), 991–1005. https://doi.org/10.1002/nme.1620100503.
Lazarus, V., 2003. Brittle fracture and fatigue propagation paths of 3D plane cracks under uniform remote tensile loading. Int. J. Fract. 122 (1–2), 23–46.
Li, S., Huang, Q., 2010. An improved form of the hypersingular boundary integral equation for exterior acoustic problems. Eng. Anal. Bound. Elem. 34 (3), 189–195. https://doi.org/10.1016/j.enganabound.2009.10.005.
Li, S., Mear, M.E., 1998. Singularity-reduced integral equations for displacement discontinuities in three-dimensional linear elastic media. Int. J. Fract. 93 (1–4), 87–114. https://doi.org/10.1023/A:1007513307368.
Li, H., Liu, C.L., Mizuta, Y., Kayupov, M.A., 2001. Crack edge element of three-dimensional displacement discontinuity method with boundary division into triangular leaf elements. Commun. Numer. Methods Eng. 17 (6), 365–378. https://doi.org/10.1002/cnm.410.
Li, L.C., Tang, C.A., Li, G., Wang, S.Y., Liang, Z.Z., Zhang, Y.B., 2012. Numerical simulation of 3D hydraulic fracturing based on an improved flow-stress-damage model and a parallel FEM technique. Rock Mech. Rock Eng. 45 (5), 801–818. https://doi.org/10.1007/s00603-012-0252-z.
Li, S., Li, X., Zhang, D., 2016. A fully coupled thermo-hydro-mechanical, three-dimensional model for hydraulic stimulation treatments. J. Nat. Gas Sci. Eng. 34, 64–84. https://doi.org/10.1016/j.jngse.2016.06.046.
Liu, S., Valkó, P.P., 2018. A rigorous hydraulic-fracture equilibrium-height model for multilayer formations. SPE Prod. Oper. 33 (02), 214–234. https://doi.org/10.2118/173335-PA.
Liu, C., Wang, X., Deng, D., Zhang, Y., Zhang, Y., Wu, H., Liu, H., 2016. Optimal spacing of sequential and simultaneous fracturing in horizontal well. J. Nat. Gas Sci. Eng. 29, 329–336. https://doi.org/10.1016/j.jngse.2016.01.024.
Maerten, F., Maerten, L., Pollard, D.D., 2014. iBem3D, a three-dimensional iterative boundary element method using angular dislocations for modeling geologic structures. Comput. Geosci. 72, 1–17. https://doi.org/10.1016/j.cageo.2014.06.007.
Mahanta, B., Tripathy, A., Vishal, V., Singh, T.N., Ranjith, P.G., 2017. Effects of strain rate on fracture toughness and energy release rate of gas shales. Eng. Geol. 218, 39–49. https://doi.org/10.1016/j.enggeo.2016.12.008.
McClure, M.W., Babazadeh, Shiozawa S., Huang, J., 2016. Fully coupled hydro-mechanical simulation of hydraulic fracturing in 3D discrete-fracture networks. SPE J. 21 (04), 1–302. https://doi.org/10.2118/173354-PA.
Meng, C., Maerten, F., Pollard, D.D., 2013. Modeling mixed-mode fracture propagation in isotropic elastic three dimensional solid. Int. J. Fract. 179 (1–2), 45–57. https://doi.org/10.1007/s10704-012-9771-6.
Miller, C.K., Waters, G.A., Rylander, E.I., 2011. Evaluation of production log data from horizontal wells drilled in organic shales. In: North American Unconventional Gas Conference and Exhibition. Society of Petroleum Engineers. https://doi.org/10.2118/144326-MS.
Nikolskiy, D.V., Mogilevskaya, S.G., Labuz, J.F., 2013. Complex variables boundary element analysis of three-dimensional crack problems. Eng. Anal. Bound. Elem. 37 (11), 1532–1544. https://doi.org/10.1016/j.enganabound.2013.08.005.
Okada, Y., 1985. Surface deformation due to shear and tensile faults in a half-space. Bull. Seismol. Soc. Am. 75 (4), 1135–1154.
Olson, J.E., 1991. Fracture mechanics analysis of joints and veins. In: Doctoral Dissertation. Stanford University.
Olson, J.E., 1993. Joint pattern development: effects of subcritical crack growth and mechanical crack interaction. J. Geophys. Res. 98 (B7), 12251–12265. https://doi.org/10.1029/93JB00779.
Peirce, A., Bunger, A., 2013. Interference fracturing: nonuniform distributions of perforation clusters that promote simultaneous growth of multiple hydraulic fractures. SPE J. 20 (02), 384–395. https://doi.org/10.2118/172500-PA.
Pollard, D.D., Aydin, A., 1988. Progress in understanding jointing over the past century Progress in understanding jointing over the past century. Geol. Soc. Am. Bull. 100 (8), 1181–1204.
Rizzo, F.J., Shippy, D.J., 1977. An advanced boundary integral equation method for three-dimensional thermoelasticity. Int. J. Numer. Methods Eng. 11 (11), 1753–1768. https://doi.org/10.1002/nme.1620111109.
Rungamornrat, J., Wheeler, M.F., Mear, M.E., 2005. Coupling of fracture/non-Newtonian flow for simulating nonplanar evolution of hydraulic fractures. In: SPE Annual Technical Conference and Exhibition. Society of Petroleum Engineers. https://doi.org/10.2118/96968-MS.
Savitzky, A., Golay, M.J., 1964. Smoothing and differentiation of data by simplified least squares procedures. Anal. Chem. 36 (8), 1627–1639.
Schöllmann, M., Richard, H.A., Kullmer, G., Fulland, M., 2002. A new criterion for the prediction of crack development in multiaxially loaded structures. Int. J. Fract. 117 (2), 129–141. https://doi.org/10.1023/A:1020980311611.
Shi, J., Shen, B., Stephansson, O., Rinne, M., 2014. A three-dimensional crack growth simulator with displacement discontinuity method. Eng. Anal. Bound. Elem. 48, 73–86. https://doi.org/10.1016/j.enganabound.2014.07.002.
Shou, K.J., Crouch, S.L., 1995. A higher order displacement discontinuity method for analysis of crack problems. Int J Rock Mech Min Sci Geomech 32 (1), 49–55. https://doi.org/10.1016/0148-9062(94)00016-V.
Shou, K.J., Siebrits, E., Crouch, S.L., 1998. A higher order displacement discontinuity method for three-dimensional elastostatic problems. Int. J. Rock Mech. Min. Sci. 2 (34), 317–322. https://doi.org/10.1016/S0148-9062(96)00052-6.
Tang, H., Winterfeld, P.H., Wu, Y.S., Huang, Z.Q., Di, Y., Pan, Z., Zhang, J., 2016. Integrated simulation of multi-stage hydraulic fracturing in unconventional reservoirs. J. Nat. Gas Sci. Eng. 36, 875–892. https://doi.org/10.1016/j.jngse.2016.11.018.
Weng, X., Kresse, O., Cohen, C.E., Wu, R., Gu, H., 2011. Modeling of hydraulic fracture network propagation in a naturally fractured formation. SPE Prod. Oper. 26 (04), 368–380. https://doi.org/10.2118/140253-PA.
Wick, T., Lee, S., Wheeler, M.F., 2015. 3D phase-field for pressurized fracture propagation in heterogeneous media. In: VI International Conference on Computational Methods for Coupled Problems in Science and Engineering, pp. 605–613.
Wu, K., 2014. Numerical modeling of complex hydraulic fracture development in unconventional reservoirs. In: Doctoral Dissertation. The University of Texas at Austin.
Wu, K., Olson, J.E., 2016. Mechanisms of simultaneous hydraulic-fracture propagation from multiple perforation clusters in horizontal wells. SPE J. 21 (03), 1000–1008. https://doi.org/10.2118/178925-PA.
Wu, Y.-S., et al., 2016. Development of non-contaminating cryogenic fracturing technology for shale and tight gas reservoirs. Project Number 10122–20.
Xiao, J., Rong, M., Li, K., Liu, X., Zhang, H., Zhu, H., 2016. 3D multi-fracture propagation modeling and perforating cluster space optimisation for the Fuling shale gas reservoir. In: SPE Asia Pacific Hydraulic Fracturing Conference. Society of Petroleum Engineers. https://doi.org/10.2118/181839-MS.
Xiong, H., 2017. Optimizing Cluster or Fracture Spacing: an Overview. https://www.spe.org/en/print-article/?art=3007.
Yew, C.H., 2007. Chapter six - turning of fracture from a deviated wellbore. In: M of H F. Gulf Professional Publishing, Houston, pp. 128–149. https://doi.org/10.1016/B978-0-88415-474-7.X5011-8.
Yew, C.H., Weng, X., 2015. Chapter two- Three-dimensional fracture modeling. In: M of H F. Gulf Professional Publishing, Boston, pp. 30–60. https://doi.org/10.1016/B978-0-12-420003-6.00002-1.
Zozulya, V., 2007. Regularization of the divergent integrals. II. Application in fracture mechanics. Electron. J. Bound. Elem. 4 (2), 58–66. https://doi.org/10.14713/ejbe.v4i2.775.